Chaos, Solitons and Fractals 182 (2024) 114701

Contents lists available at ScienceDirect

Chaos, Solitons and Fractals

journal homepage: www.elsevier.com/locate/chaos

First- and second-order phase transitions in electronic excitable units and neural dynamics under global inhibitory feedback

Ludovico Minati [a,b,*], Silvia Scarpetta [c,d], Mirna Andelic [e,f], Pedro A. Valdes-Sosa [a,g], Leonardo Ricci [h], Antonio de Candia [i,d]

[a] School of Life Science and Technology, University of Electronic Science and Technology of China, 611731 Chengdu, China
[b] Center for Mind/Brain Sciences (CIMeC), University of Trento, 38123 Trento, Italy
[c] Department of Physics "E.R. Caianiello", University of Salerno, 84084 Fisciano (Salerno), Italy
[d] INFN Gr. Coll. Salerno, Naples Unit, 84084 Fisciano (Salerno), Italy
[e] Neuroalgology Unit, "Carlo Besta" IRCCS Institute Foundation, 20133 Milan, Italy
[f] School of Mental Health and Neuroscience, Maastricht University Medical Centre, 6202 AZ Maastricht, The Netherlands
[g] Department of Neuroinformatics, Cuban Neuroscience Center, 11600 Havana, Cuba
[h] Department of Physics and Center for Mind/Brain Science (CIMeC), University of Trento, 38123 Trento, Italy
[i] Department of Physics "E. Pancini", University of Naples "Federico II", 80126 Napoli, Italy

ARTICLE INFO

Dataset link: http://dx.doi.org/10.5281/zenodo.10585140

Keywords:
Bistability
Global inhibition
Hysteresis
Neural systems
Neon glow lamp
Phase transition

ABSTRACT

The diverse roles of inhibition in neural circuits and other dynamical networks are receiving renewed interest. Here, it is shown that increasing global inhibitory feedback leads to gradual rounding of first-order transition between dynamical phases, turning it into second-order transition. The effect is initially observed in an electronic model consisting of a bi-dimensional array of neon glow lamps, where global inhibition can be simply introduced through a resistor in series with the supply voltage. The experimental findings are confirmed using both an extended numerical model and a mean-field approximation, then replicated across different models of neural dynamics, namely, the Wilson–Cowan model and a network of leaky integrate-and-fire neurons. Across all these systems, a critical point is always found as a function of a pair of parameters controlling local excitability and global inhibition strength, and a general explanation revealing the roles of the shape of the activation function and voltage fluctuations versus the extinction time-scale is provided. It is speculated that the brain could use global inhibition as a versatile means of shifting between first- and second-order dynamics, addressing the conundrum regarding the coexistence in neural dynamics of phenomena stemming from both. Some reflections regarding the comparison with other physical systems and the possible physiological significance are offered, and a hypothetical setup for an optogenetics experiment on cultured neurons is put forward.

1. Introduction

1.1. Inhibition and global inhibition in neural systems

The development of experimental neurophysiology and computational neuroscience has been permeated by the notion that sensorimotor and cognitive functions in the brain rely primarily on excitatory neurons, to the point of them being referred to as "principal neurons" [1,2]. As the name implies, until recently interneurons have generally been considered ancillary in-betweens providing a nonspecific blanket of inhibition. Their function has largely been assumed to consist of balancing activity around an optimal point allowing neural coding and computation to take place [3]. This view originated partly from the lower prevalence of inhibitory neurons, on the order of 10%–30% of the total depending on the region, and partly from the postulate, largely refuted by recent results, that interneurons are phenotypically less differentiated than excitatory neurons. It is now established that, aside from their role in the excitation–inhibition balance, interneurons are functionally specialized and enjoy considerable diversification across cortical regions with specific architectural arrangements [4,5]. There is, therefore, an interest in further elucidating the structural and functional aspects of inhibition.

According to current knowledge, inhibition in the brain primarily involves three configurations [6]. First, feedback inhibition, which acts

* Corresponding author at: School of Life Science and Technology, University of Electronic Science and Technology of China, 611731 Chengdu, China.
E-mail addresses: lminati@uestc.edu.cn, ludovico.minati@unitn.it, lminati@ieee.org (L. Minati).

https://doi.org/10.1016/j.chaos.2024.114701
Received 30 January 2024; Accepted 3 March 2024
Available online 18 March 2024

locally at the microcircuit level to provide a negative loop term, implemented via direct interconnections between excitatory neurons, such as pyramidal neurons, and the interneurons geometrically intertwined with them. It mainly underpins the dynamical maintenance of the excitation–inhibition balance supporting operation close to criticality, with profound implications for information storage and processing [7,8]. Second, lateral inhibition, consisting of a topographically patterned feedback architecture at the mesoscale, wherein inhibition applies a sharpening function to the neural receptive fields and supports pattern formation. It plays a role in implementing perceptual processing and higher functions, though its influence remains to be fully clarified [9]. Third, feedforward inhibition, which acts at the macroscopic level, for example inter-hemispherically, wherein distant cortical regions inhibit each other via projection connections. A well-studied example is the antagonistic relationship between activation in the left and right motor cortex [10].

In a testament to the diversification and complexity of inhibitory neurons, a recent microscopy study revealed that a single interneuron in the mouse visual thalamus possesses as many as 899 synaptic inputs and 623 outputs, and its neurites span more than half of the visual field [11]. This strikingly high in- and out-degrees for a single neuron point to its involvement in gathering information about the overall state of a pool of excitatory neurons, and distributing a form of global inhibitory feedback (in short, global inhibition). In other words, while inhibitory feedback may be calculated and delivered over small groups of neurons, there is biological evidence that it is also implemented on a considerably larger scale [12].

A well-studied example of global inhibition is that of head-direction cells, which are neurons that fire selectively as a function of the heading with respect to a landmark. As demonstrated both numerically and experimentally, their dynamics are modeled by ring attractor networks, where a localized bump of activity is sustained by the interplay between local excitation and global inhibition [13–15]. Another domain in which global inhibition plays a key role is the maintenance of sparse representations, such as those encoding odors through glomerular activation in insects. In that context, it is implemented by interneurons that act locally on principal cells but receive non-selective and ubiquitous excitatory inputs; accordingly, inhibiting their action profoundly alters the coding specificity [16,17]. A role in coding sparsification and thus the maximization of information capacity has been demonstrated more generally in computational neural models [18]. Global inhibition has also been implicated in memory retrieval, wherein its strength allows versatile control of the recall range within arbitrary graph structures [19]. Moreover, in an apparent paradox, it can facilitate signal amplification at the network level due to its influence on the eigenspectrum [20].

1.2. Electronic model of the influence of global inhibition on transition order

In this paper, global inhibition is investigated from a further perspective, that is, its influence on the transitions between dynamical regimes. While the study of neural activity across levels of scale from the perspective of statistical physics has run through more than two decades, there remain open questions regarding these transitions [21]. On the one hand, signatures of first-order transition are found in the bistability and hysteresis exhibited behaviorally and neurophysiologically, which, for example, support short-term memory persistence, attention and task performance, as well as the formation of perceptual priors [22–25]. Bistability (more generally, multistability) and hysteresis are also a common observation in the intrinsic dynamics of brain networks and in the interactions between neural activity and other physiological systems [26,27]. On the other hand, substantial in-vivo and in-vitro evidence from the spatiotemporal distribution of neural activity suggests preferential operation in the vicinity of a critical point, implying second-order transition. The scale-free distributions of avalanche size and duration are a well-established experimental fact and, albeit indirectly, credible signatures of (near) criticality have also been obtained from macroscopic recordings of brain activity, including haemodynamics and electroencephalography [28–31]. It has been posited that criticality emerges through a self-organization process and represents a fundamental feature of neural activity, in that it optimizes the dynamical range, information capacity and transmission, and ability to switch between learned patterns [32–36]. First- and second-order transitions, therefore, seem to coexist in several aspects and across levels of brain dynamics, underlying the presence of large numbers of metastable states [37,38].

In the past, we proposed an elementary analog electronic circuit based on gas discharge tubes (specifically, neon glow lamps), which recapitulated this coexistence in the form of a hysteretic transition between two dynamical regimes endowed with different intensities of activity and levels of spatiotemporal order. In the proximity of the spinodal line, precursors of critical behavior could be clearly observed [39]. Later, closely similar effects were replicated in a network of leaky integrate-and-fire neurons whose connections encoded learned spatiotemporal patterns [40]. Throughout this paper, after a brief summary of the electronic model, we introduce a simple extension of the circuit, consisting of introducing a single resistor which, via Ohm's law, effectively implements a form of global inhibition. The effect of this feedback, namely to gradually shrink the hysteresis region, round and eventually abolish the discontinuous transition, is demonstrated both numerically and experimentally. A mean-field model is then used to assert the generalizability of the findings, which is in turn demonstrated in the context of the Wilson–Cowan model and a network of leaky integrate-and-fire neurons. The possible physiological underpinnings and broad implications are discussed, particularly regarding global inhibition as a possible versatile means for the brain to shift between first- and second-order transition dynamics. Finally, a biological experiment is proposed.

2. Experiments on a bidimensional array of neon lamps

2.1. Apparatus and data acquisition

Neon glow lamps (in brief, neon lamps), consist of sealed glass vessels containing a neon-argon mixture and two cylindrical electrodes. Despite their inconspicuous appearance, the richness of their physics is readily observable through their tendency to spontaneously flicker in complex temporal patterns. On the one hand, their behavior is strongly hysteretic, as the voltage required to initiate the discharge is markedly higher than the one needed to maintain it, mainly due to the influence of the ionization state of the gas. On the other hand, in the vicinity of the striking and extinction voltages, the corresponding transitions, referred to as breakdown and recovery, are stochastic according to markedly voltage-dependent probabilities. Additional non-idealities include long-term memory due to the residual ionization even after extinction, aging, eventually polarization, and light sensitivity [41]. While now largely relegated as inexpensive line voltage indicators, these devices once played a notable role in the design of oscillators and even logic circuits, and their importance as a non-linear circuit element is demonstrated in the early observations by van der Pol of chaotic behavior [42].

As detailed in Ref. [39], inspired by these properties, by the Pearson–Anson oscillator [43] and its derivatives including capacitively-coupled loops that give rise to sequential flashing, a bi-dimensional array was designed. Each unit consists of a lamp with one terminal connected to a global node A (typically, towards a positive voltage) via a resistor of value R and the other terminal connected to another global node B (typically, towards ground). All intermediate terminals between the lamps and resistors are interconnected via capacitors of value C arranged as a grid according to Von Neumann neighborhood (Fig. 1a). An important difference with respect to Ref. [39] is that in this study periodic boundary conditions are implemented in the connections of

both rows and columns, so that, for instance, element $(1,1)$ is coupled to $(1,32)$ and $(32,1)$. This removes effects related to the distance from the boundary, which amplify the dependence of the observations on the system size. Throughout this paper, particular emphasis is placed on considering this entire circuit as a self-contained two-terminal device, referred to as X1, showing a strikingly complex voltage-current-time dependence.

The apparatus, consisting of a 32×32 array, was realized using lamps type NE-2C or equivalent, assembled on a printed circuit board and enclosed in a black polyurethane shield to attenuate ambient light and prevent optical cross-talk between adjacent nodes (Fig. 2a). For these lamps, the typical breakdown and recovery voltages are, respectively, on the order of $v_B \approx 76$ V and $v_R \approx 61$ V; however, these are sensitive to aging and polarization effects. The value of the resistors was set to $R = 2.2$ MΩ and that of the capacitors was set to $C = 220$ nF, giving a characteristic time constant of $\tau = RC = 0.48$ s. For specific experiments, the system size was reduced by removing all the resistors and capacitors in contiguous rows of the array. The apparatus was housed in a sealed dark chamber at a temperature around 21 °C.

In Ref. [39], the spontaneous behavior of this system as a function of the externally-applied DC voltage V_s was initially investigated. Throughout this paper, the focus is on the influence of an additional resistor of value R_0 globally connected in series to the voltage source. Via Ohm's law, this component provides an instantaneous feedback mechanism reducing by $R_0 i(t)$ the voltage across X1 as a function of the current $i(t)$ flowing through it. A dedicated circuit providing the adjustable DC voltage, allowing changing R_0 and measuring the time course of $i(t)$ was designed (Fig. 1b). The voltage set-point was emitted by a digital to analog converter U1, filtered by a low-pass filter comprising R1 and C2, and entered into a feedback amplifier U2, which provided the control signal for a step-up converter U3 through resistors R2 and R3. The voltage V_s was in turn filtered through a capacitor C1 and applied to the device X1, which was connected to the ground via a small resistor R4 and a variable resistor R5, adjusted to realize the value R_0. The current $i(t)$ was read out through the voltage drop across R4 via an instrumentation amplifier U4, and finally digitized using an oscilloscope X2.

These circuits were realized on a separate plugboard (Fig. 2b), connected via a BNC cable to the array board and to an external fixed ±15 V power supply, and carrying a microcontroller board type Arduino Nano as interface to the computer controlling the experiment. The digital to analog converter U1, driven by said microcontroller, had a resolution of 16 bits, type MAX541 or equivalent, whereas R1 and C2 had values 15 kΩ and 1 μF, respectively. The amplifier U2, type TL072 or equivalent, was connected to R2 and R3, having values 270 kΩ and 1 kΩ. The converter U3, type A02P-5A or equivalent, powered by a type 7805 or equivalent linear regulator, had its output connected to four 2.2 μF ceramic capacitors in parallel, represented by C1. The current-sensing resistor R4 had value 10 Ω, and the potential drop across it was amplified by a gain of 365 by the instrumentation amplifier U4, type AD620 or equivalent, before being digitized at 8 bit, 100 kSa/s by the oscilloscope X2. The variable resistor R5, iteratively adjusted to the required values of R_0, was implemented firstly with a digital potentiometer, type AD7376A10 or equivalent, then replaced with a manually-adjusted trimmer to reduce parasitic effects. Additional circuits for overvoltage protection, health monitoring, and controllable polarity inversion were provided but are omitted for brevity. The duration of each recording was set to 5 s. All time-series data have been publicly released and are downloadable from Ref. [44]. For specific recordings, the activity within X1 was also optically observed using a CMOS camera having a frame rate of 25 Hz.

2.2. Effects of series resistance and system size

While performing a first voltage cycle applying series resistance $R_0 = 0$ Ω, in steps of $\delta V_s = 0.05$ V for 5 s each, a marked hysteresis

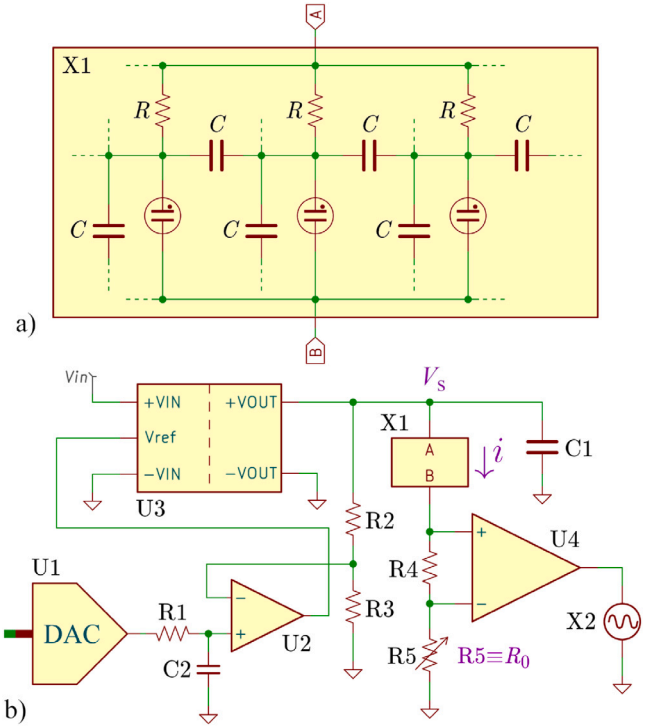

Fig. 1. Circuit diagrams of the experimental apparatus. (a) Internal structure of the 32×32 bidimensional array of neon lamps with periodic conditions, observed as a two-terminal device X1 (three-node subset shown for convenience). (b) Simplified schematic of the driving and readout electronics, denoting the applied voltage V_s, global series resistance R_0 and measured current i.

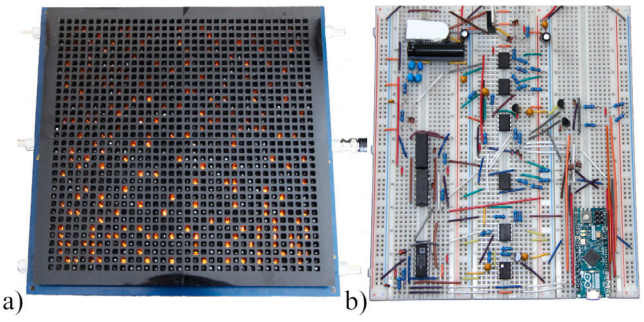

Fig. 2. Physical implementation. (a) Bidimensional array of neon lamps including the optical shield. (b) Realization of the supporting circuits on a plugboard.

effect was noticeable, with a sharp transition to a high-rate state, and a more gradual decay of activity as the voltage was decreased (Fig. 3a). Integrating the area of the loop from the bottom, the voltages corresponding to the upward and downward transitions at the level corresponding to half of the total area were calculated. These were $v_{up} = 69.95$ V and $v_{down} = 68.85$ V, corresponding to a hysteresis in the effect of the control voltage of $\Delta V_s = 1.1$ V. Due to multiple factors including the probabilistic nature of the transitions and the generation within the array of voltages higher than V_s, generally v_{up} and v_{down} do not coincide with v_B and v_R; in other words, the ignition–extinction hysteresis exhibited by each lamp is a physically different phenomenon compared by the bistability in the collective activity. Owing to the different rates of increase and decay of the activity, the loop appeared pinched at the top-right; the frequency at the pinching point was empirically determined as the highest rate for which $f_{down} - f_{up} > 10$ Hz, giving $f_p = 320.6$ Hz. The system behavior was similar to that observed in Ref. [39], wherein the focus was on critical phenomena occurring

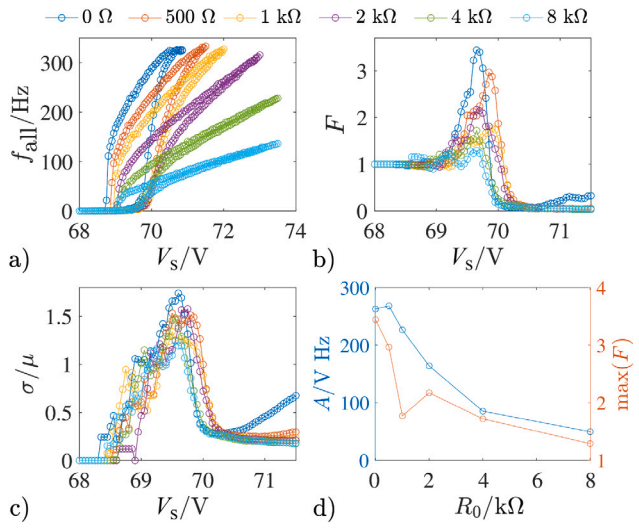

Fig. 3. Experiments on the effect of the global series resistance R_0. (a) Overall event rate f_{all} as a function of the applied voltage V_s during closed loops for different settings of R_0. (b) and (c) Corresponding Fano factor F and coefficient of variation σ/μ (increasing voltage, smoothing applied). (d) Loop area A and maximum Fano factor $\max(F)$ as a function of R_0.

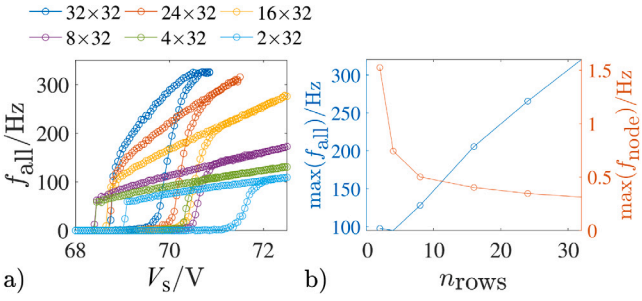

Fig. 4. Experiments on the effect of the system size in terms of the number of rows n_{rows}. (a) Overall event rate f_{all} as a function of the applied voltage V_s during closed loops for different settings of n_{rows}. (b) Overall and individual event rates $\max(f_{all})$ and $\max(f_{node})$ corresponding to the pinch point of the loops, as a function of n_{rows}.

in the vicinity of the transition from low-rate activity, referred to as phase I, to high-rate activity, referred to as phase II, corresponding to f_p. The small discrepancy in v_{up} and v_{down} was plausibly down to aging of the lamps due to the time span of several years between the two experiments.

As the series resistance was increased, the maximum rate remained relatively unaltered up to $R_0 = 1$ kΩ, then decreased rapidly, with $f_p = \{320.6, 318.2, 310.5, 265.6, 152.4, 66.3\}$ Hz for $R_0 = \{0, 0.5, 1, 2, 4, 8\}$ kΩ. Furthermore, the morphology of the loop gradually changed. The transition to high rate became less sharp, with the rate around $v_{up} \pm 0.1$ V steadily decreasing, even for the first three settings of R_0, across which f_p remained relatively unaltered, with $\Delta f_{all}/\Delta V_s = \{552.0, 357.7, 287.0, 176.3, 104.7, 53.0\}$ Hz/V. This rounding brought the increasing and decreasing trends closer, contributing to a gradually reduced loop area, with $A = \{261.2, 268.2, 226.3, 163.8, 152.4, 66.3\}$ V Hz; eventually, for $R_0 = 8$ kΩ, the trends overlapped substantially, leaving only a small fraction of the initial loop area and largely removing the discontinuities hallmarking the first-order phase transition observed in the initial study of this system. Accordingly, the width of the loop at the height corresponding to half-area consistently shrank, with $\Delta V_s = \{1.1, 1.15, 1.05, 0.85, 0.6, 0.6\}$ V.

To tentatively address the question of whether the first-order transition observed in the absence of series resistance (i.e., $R_0 = 0$ Ω) changed into a second-order transition, or simply faded into a continuous change, signatures of criticality were searched for by calculating the Fano factor. Given event counts n_k over time bins $k = 1 \cdots n_{bins}$ of width δ_{bin}, it is defined as

$$F = \frac{\langle n_k^2 \rangle - \langle n_k \rangle^2}{\langle n_k \rangle}. \quad (1)$$

Initially introduced in nuclear physics as a statistical measure of the ionization produced by charged particles [45], this measure has become widely used, particularly in neuroscience [21,46,47], as a proxy indicator of the divergence of fluctuations anticipated close to the critical point. If the event count is extracted from a Poissonian distribution $P(n) = \frac{\mu^n}{n!} e^{-\mu}$, where $\mu = \rho(t)\delta_{bin}$ and $\rho(t)$ is constant over time, then $F = 1$. For temporally clustered events such as avalanches, the overdispersion reflects into $F > 1$.

Following Ref. [39], let $n_{bins} = 20$, corresponding to a width of $\delta_{bin} = 0.25$ s, well within the scaling region previously observed; to enhance the accuracy of determining F for relatively short time series, the standard deviation σ and mean μ of the event counts were independently determined 10 times, shifting the bin positions by the corresponding fractions, and the resulting values of F were averaged. As expected, while in phase I at voltages well below the transition, the activity was essentially Poissonian, with $F \approx 1$. In the vicinity of the transition phase I→II, signatures of criticality emerged and could be seen in the form of a peak in F as a function of V_s (Fig. 3b). For higher voltages, within phase II, the activity was highly ordered, which reflected in $F \approx 0$. However, the peak value of the Fano factor, rather than increasing as would be expected when approaching the critical point, gradually decreased for increasing R_0, with $\max(F) = \{3.44, 2.97, 1.77, 2.17, 1.72, 1.29\}$. Analogous results, not reported for brevity, were obtained for the other settings of the bin width considered in Ref. [39]. The trend closely followed the shrinkage of the loop area (Fig. 3d). Crucially, this situation should not be interpreted as evidence for the absence of a second-order transition, and these interim results are specifically reported to warn about this fact. As will be clarified by the numerical results presented in the Section 3, the issue is that there is a fundamental difference in time-scale between the transition precursors, studied in Ref. [39] and which result in the peak of the Fano factor with increasing V_s, and the dynamics in the vicinity of the critical point. In the latter case, the increased autocorrelation time implies the need for substantially longer bin sizes to capture the very slow fluctuations in the event rate, which would not be compatible with experimental observation using the present apparatus due to the resulting time series length and practical factors such as the long-term stability of the setup. For completeness, as a further measure of regularity, the coefficient of variation in the inter-event intervals δt_i was calculated as $\sigma(\delta t_i)/\mu(\delta t_i)$. The corresponding peak values $\max(\sigma(\delta t_i)/\mu(\delta t_i)) = \{1.74, 1.53, 1.34, 1.58, 1.48, 1.24\}$ did not show a clear trend as a function of R_0 (Fig. 3c).

Observing the decrease in rate as a function of series resistance, the question arises of whether similar effects could be obtained by reducing the system size. For practical reasons, reducing the number of array columns was problematic, so this was investigated by removing nodes through disconnecting entire rows, resulting in $n_{rows} = \{32, 24, 16, 8, 4, 2\}$. The corresponding rate gradually decreased, with $f_p = \{320.6, 265.6, 205.7, 128.2, 95.1, 97.6\}$ Hz (Fig. 4a). Notably, when normalizing the rate by the number of nodes, a more than three-fold increase was observed, indicating that the individual flashing frequency became higher, which could be viewed as an attempt to "compensate" the reduced system size (Fig. 4b). While reducing n_{rows}, the morphology of the loop also changed, however, intriguingly, the hysteresis effect become more, rather than less evident (Fig. 4a). Accordingly, the reduction in the area appeared less marked compared to the effect of R_0, with $A = \{261.2, 271.1, 270.7, 215.8, 152.7, 200.6\}$ V Hz and the width of the loop at the height corresponding to half-area increased rather than decreased, with $\Delta V_s = \{1.1, 1.35, 1.75, 2.15, 1.9, 2.5\}$ V. The peak value of the Fano factor featured no discernible trend, with $\max(F) =$

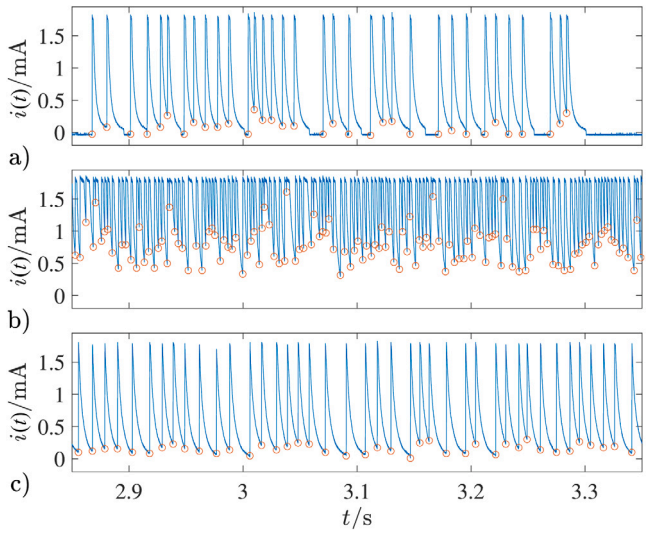

Fig. 5. Representative snippets of current $i(t)$ waveform recordings for (a) applied voltage $V_s = 69.7$ V and series resistance $R_0 = 0$ Ω, (b) $V_s = 70.2$ V and $R_0 = 0$ Ω, (c) $V_s = 70.2$ V and $R_0 = 4$ kΩ. Orange circles denote the detected events.

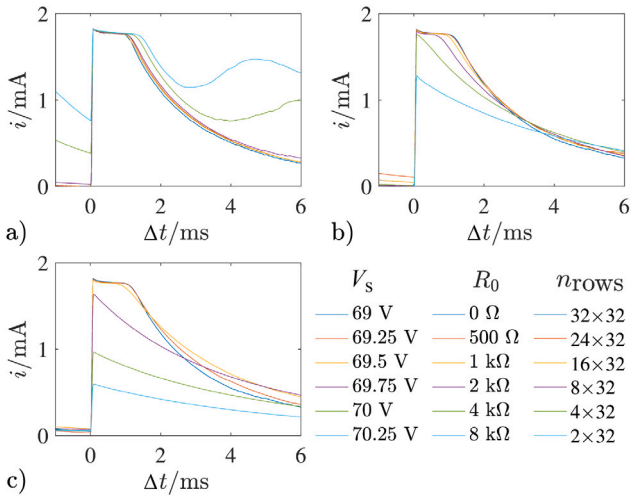

Fig. 6. Recorded time-locked averaged current $i(\Delta t)$ waveforms, whereby $\delta t = 0$ corresponds to event onset. (a) As a function of the applied voltage V_s, for series resistance $R_0 = 0$ Ω and system size $n_{rows} = 32$. (b) As a function of R_0, for $V_s = v_t$ corresponding to $f'_{all} = \max(f'_{all})$ and $n_{rows} = 32$. (c) As a function of n_{rows}, for $V_s = v_t$ and $R_0 = 0$ Ω.

$\{3.44, 5.04, 2.96, 3.93, 4.74, 5.5\}$. In this experiment, the effect of reducing the system size was, therefore, different compared to the influence of increasing the global series resistance R_0. However, as demonstrated by the numerical results in the Section 3, the effect becomes analogous if all units in the array are assumed to be identical.

2.3. Qualitative aspects

Additional information about the influence of the global series resistance R_0 could be obtained by considering qualitative aspects of the spatiotemporal dynamics. In the case of $R_0 = 0$ Ω, while in phase I for $V_s = 69.7$ V, the system generated clearly distinct peaks of current absorption, characterized by a sharp increase, followed by a plateau and an exponential decrease; the events only partially overlapped in their exponential tails, resulting in the reading spending the majority of time around $i \approx 0$ mA (Fig. 5a). By contrast, in phase II for $V_s = 70.2$ V, the rate of event generation was considerably higher, resulting in substantial overlap of adjacent events; accordingly, the reading spent the majority of time around $i \approx 1.75$ mA, effectively representing a saturation current, and the events were detectable as drops from this level (Fig. 5b). For sufficiently large settings of the series resistance, e.g. $R_0 = 4$ kΩ, in phase I for $V_s = 70.2$ V, the morphology of each spike appeared modified, as the exponential decay started immediately after the initial increase (Fig. 5c).

The further elucidate this effect, the time-locked response of the current in the neighborhood of each event was calculated. In the absence of series resistance, i.e. $R_0 = 0$ Ω, and with full system size, i.e. $n_{rows} = 32$, each event consisted of a rapid increase from $i(\Delta t) \approx 0$ mA to $i(\Delta t) \approx 1.75$ mA within $\Delta t \approx 0.07$ ms, followed by a plateau lasting ≈ 1 ms with minimal voltage drop, and finally an exponential decay. For voltages below $V_s = 70$ V, for which transition to phase II occurred, the exponential decay rate remained clearly insensitive to the voltage, with $\lambda = \{0.41, 0.4, 0.4, 0.39\}$ ms^{-1} for $V_s = \{69, 69.25, 69.5, 69.75\}$ V (Fig. 6a).

The situation appeared markedly different as regards the effect of the global series resistance R_0, charted considering the voltage $V_s = v_t$ corresponding to the largest positive first derivative $f'_{all} = \max\left(f'_{all}\right)$; this setting was not critical, and similar results would be obtained for other values in phase I with sufficient events. For $R_0 = \{0, 0.5, 1\}$ kΩ, the plateau at $i(\Delta t) \approx 1.75$ mA remained essentially unaltered. For $R_0 = 2$ kΩ, it was reduced down to ≈ 0.5 ms, and for $R_0 = \{4, 8\}$ kΩ, it disappeared, with the exponential decay starting immediately after an initial peak, which reached, respectively $i = \{1.76, 1.28\}$ mA. The exponential decay rate dropped markedly over the span of R_0, with $\lambda = \{0.38, 0.36, 0.35, 0.31, 0.26, 0.19\}$ ms^{-1} (Fig. 6b). These changes were a consequence of the feedback mechanism realized by the series resistor, which instantaneously reduced the applied voltage following an increase in current. In particular, the shallower response with higher values of R_0 attenuated the amount of spatiotemporal variance provided to the array by each event, as will be explicitly represented by decreasing values of the variance "quantum" parameter ϵ in the mean-field model introduced in Section 4.

The effect of the system size n_{rows}, again charted considering the voltage $V_s = v_t$, appeared notably similar to that of the global series resistance R_0. For $n_{rows} = \{32, 24, 16\}$, the plateau at $i(\Delta t) \approx 1.75$ mA remained largely unaltered; by contrast, for $n_{rows} = \{8, 4, 2\}$, it disappeared, and the exponential decay started immediately after an initial peak, which reached $i = \{1.64, 0.97, 0.59\}$ mA. The exponential decay rate markedly dropped over the span of n_{rows}, with $\lambda = \{0.38, 0.34, 0.28, 0.22, 0.18, 0.17\}$ ms^{-1} (Fig. 6c). These changes reflected the observation that the light flashes tended to be weaker when the system size was decreased. Overall, these results revealed that, even though at the level of the hysteresis loop the influences of the series resistance and system size were different, at the underlying level of the dynamics of individual events their effects were indeed similar, in line with the simulations reported in Section 3.

While so far the behavior of the apparatus was considered through its voltage-current response as if it were a two-terminal non-linear device X1, that is, a black box, additional insight could be obtained by observing its internal dynamics, in particular, the spatial distribution of the event rate (Fig. 7). In the absence of the series resistor, i.e. $R_0 = 0$ Ω, during a voltage cycle in steps of $\delta V_s = 0.05$ V for 5 s each, the fraction of active nodes p, intended as those having $f_{node}(i, j) > 0$, approached unity, with $p = \{0.50, 0.92, 0.98, 0.99, 0.98, 0.94, 0.87, 0.67\}$ for $V_s = \{68.3, 68.85, 69.4, 69.95, 69.5, 68.95, 68.4, 67.85\}$ V. For the higher values of series resistance, the situation was substantially different: at $R_0 = 8$ kΩ, the fraction of active nodes was $p = \{0.00, 0.22, 0.30, 0.37, 0.33, 0.25, 0.16, 0.00\}$. In other words, increasing the series resistance had not only the influence of reducing the event rate of each node but also had the spatial effect of entirely obliterating large portions of the array. Notably, while in the case of $R_0 = 0$ Ω for low voltages the inactive nodes were scattered homogeneously across the array,

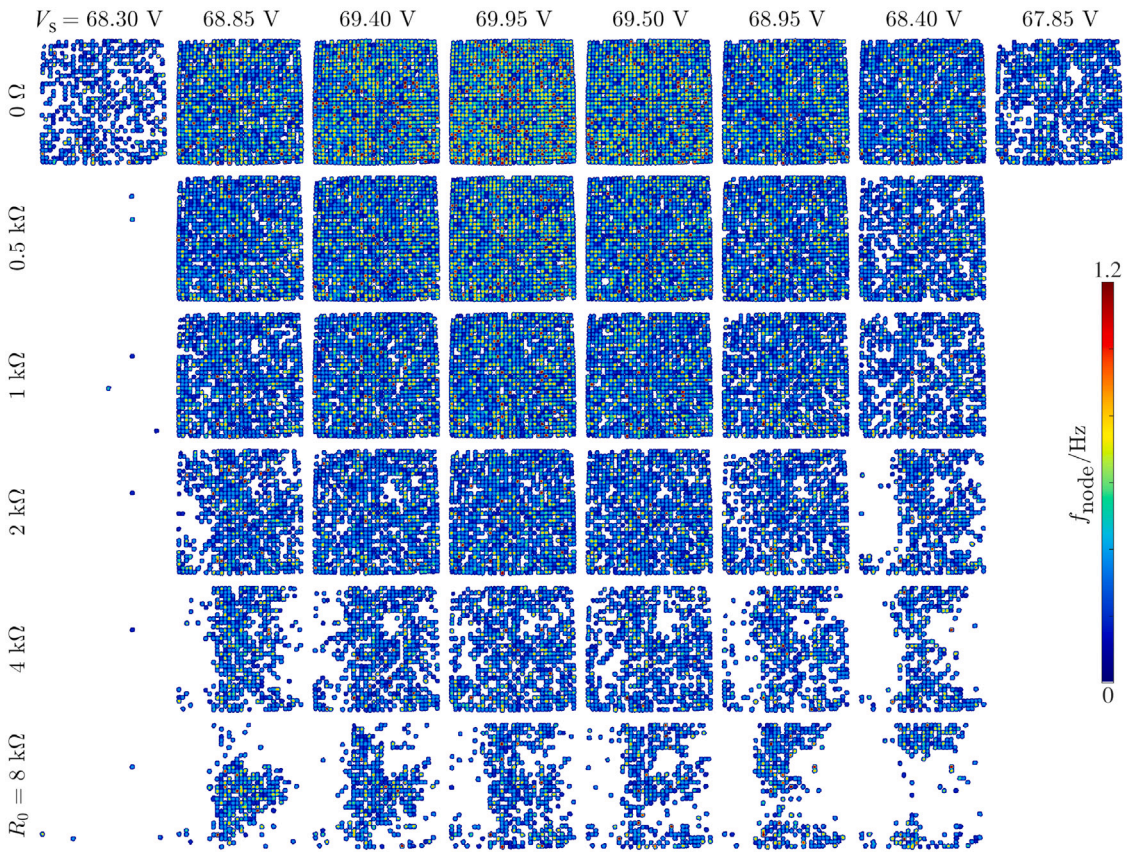

Fig. 7. Individual event rate f_{node} maps from video recordings, shown as a function of the applied voltage V_s and series resistance $R_0 = 0$ Ω. Inactive nodes ($f_{node} = 0$ Hz) omitted and left blank.

for $R_0 = 8$ kΩ at all voltages, large contiguous regions of the array were entirely inactive. Evidently, this was related to the presence of spatial heterogeneities in the array, essentially a form of "frozen variance", stemming from the heterogeneities in the values of the resistances, capacitances and breakdown voltages, on the order of 1–10%. Interestingly, the active nodes tended to be grouped together into a large cluster, the shape and location of which changed with the applied voltage. The gradual drop in number of active sites due to the growth of these inactive regions was particularly well-evident at voltages close to $v_{up} = 68.85$ V and $v_{down} = 68.4$ V, with, respectively, $p = \{0.92, 0.86, 0.78, 0.60, 0.38, 0.22\}$ and $p = \{0.87, 0.71, 0.62, 0.41, 0.27, 0.16\}$. The gradual growth and merging of these inactive regions with increasing resistance appeared reminiscent of a nucleation-like effect, which, while generally associated with first-order transitions, ensued for large resistor values [48].

2.4. Commentary

To summarize, these experiments demonstrated that the additional resistor connected in series to the voltage supply, thus implementing a global negative feedback, fundamentally altered the qualitative features of the transition between the two phases of the system. In the absence of this resistor, the transition was discontinuous and exhibited considerable hysteresis, and was thus of the first-order type. As the value of this resistor was elevated, the discontinuity gradually disappeared, with a shrinkage of the hysteresis region and a rounding of the discontinuity, leading to a continuous effect plausibly reflecting second-order transition. As discussed in Section 6, these findings are reminiscent of recent results on the shifting in a continuum between first- and second-order phase transition observed in brain dynamics [25]. Throughout the following sections, the nature of this effect is revealed, first using an extended numerical model, and then via a suitable mean-field approximation. A detailed analysis of the further effects that were observed, especially nucleation, and of the influence of unit heterogeneity, while necessary for a complete understanding of these experiments, is left for others to pursue.

3. Extended numerical model of the array of neon lamps

3.1. Model specification

To gain further insight into the mechanisms underlying the observed phenomena, and to ensure they did not arise spuriously due to non-ideal behavior of the experimental apparatus, extensive simulations of an event-based model were conducted. The model, initially introduced in Ref. [39], consists, as the experimental setup in Section 2, of a 32×32 square bidimensional array comprising $N = L^2$ units, indexed with $k = 1 \dots N$. Let the neon lamps be represented as independent and identical binary units, which can be either in "off" or "on" state; this is a reasonable first-order approximation of their physical behavior [41]. Each lamp functions as an open circuit having zero conductance $\sigma_k = 0$ while in the "off" state, and as a positive DC source of a voltage $F_k = F$ with a finite conductance $\sigma_k = \sigma$ while in the "on" state. As in Section 2, let two given nodes i and j be connected via a capacitor $C_{ij} = C$ if they are first neighbors on the array according to Von Neumann neighborhood and closed boundary conditions, with $C_{ij} = 0$ otherwise.

Let us consider the same node circuit as in Fig. 1a. Then,

$$i_k^{(R)}(t) = \frac{v_0(t) - v_k(t)}{R} \tag{2}$$

denotes the currents flowing through the kth node resistors having value R, where $v_0(t)$ is the voltage at the point of connection between the global series resistance R_0 and said node resistors, and

$$i_k^{(L)}(t) = \Delta_k \sigma_k (v_k(t) - F) \tag{3}$$

denotes the currents through the kth lamps, where $\Delta_k = \{0, 1\}$ depends on the state ("off" or "on") of the same. Therefore, $i_k^{(C)}(t) = i_k^{(R)}(t) - i_k^{(L)}(t)$ is the overall current flowing out through the capacitors from the kth node to its four neighbors.

In the absence of changes in the lamp states, the node potentials $v_k(t)$ evolve continuously according to the N equations

$$\frac{\mathrm{d}}{\mathrm{d}t} \sum_j C_{ij} \left[v_i(t) - v_j(t) \right] = i_i^{(C)}(t). \tag{4}$$

Via Kirchhoff's current law, the following equations hold,

$$\sum_k i_k^{(R)}(t) = \sum_k \frac{v_0(t) - v_k(t)}{R} = i_0(t), \tag{5a}$$

$$\sum_k i_k^{(L)}(t) = \sum_k \Delta_k \sigma_k (v_k(t) - F) = i_0(t), \tag{5b}$$

where $i_0(t) = [V_s - v_0(t)]/R_0$ is the current flowing through the global series resistor having value R_0, which implements the inhibitory feedback as discussed above. For the avoidance of confusion, here $i_0(t)$ corresponds to $i(t)$ in Section 2, examples of which are plotted in Fig. 5. Given that the N equations (Eq. (4)) are mutually linearly dependent, one can choose any $N - 1$ of them, so that, alongside the other two equations (Eq. (5)), they form a set of equations for the $N + 1$ variables $v_0(t), v_1(t), \ldots, v_N(t)$, that can be integrated during the time intervals when the lamp states do not change.

When the state of one lamp changes, and therefore some Δ_k switches from 0 to 1 or vice-versa, the potential $v_0(t)$ exhibits a discontinuity Δv_0, and all the N potentials $v_1(t), \ldots, v_N(t)$ have the same discontinuity $\Delta v_1 = \cdots = \Delta v_N$. Such discontinuities can be computed from the equations (Eq. (5)), and it should be borne in mind that $\sum_k i^{(C)}(t) = 0$. The switching is modeled as a stochastic event occurring with a rate depending exponentially on the potential across each lamp; namely, the transition from "off" to "on" takes place with a rate $\lambda_k = \rho_{on} \exp\left(\frac{v_k(t) - V_{on}}{D_{on}}\right)$, whereas that from "on" to "off" takes place with a rate $\bar{\lambda}_k = \rho_{off} \exp\left(\frac{V_{off} - v_k(t)}{D_{off}}\right)$ (n.b., V_{on} and V_{off} here correspond to V_B and V_R in Section 2, but are indicated differently to emphasize that they are not experimental measurements but parameters of an idealized model).

In keeping with Ref. [39] and with the experimental setup in Section 2, the parameters were set as follows: node resistor value $R = 2$ MΩ, coupling capacitance $C = 220$ nF, lamp equivalent conductance $\sigma^{-1} = 2.7$ kΩ and series DC voltage $F = 55$ V, transition rates $\rho_{on} = \rho_{off} = 1$ ms^{-1}, characteristic breakdown and recovery voltages $V_{on} = 76.2$ V and $V_{off} = 61.3$ V, with corresponding scaling coefficients $D_{on} = D_{off} = 0.4$ V. It is important to underline a fundamental difference with respect to the experimental case, namely, that all units were assumed to be identical across the nodes. The size of the square array was varied between $L = 20$ and $L = 32$ (in the absence of experimental constraints, unlike in Section 2, here the extent of both dimensions of the array was varied conjointly), and the global resistance was swept over $R_0 \in [0, 8]$ kΩ.

To realize the event-related simulation, the following steps were iterated:

- For each unit, the time $\hat{t}_k > t$ of the next transition was drawn from a Poissonian distribution $P(\hat{t}_k) = \lambda_k e^{-\lambda_k(\hat{t}_k - t)}$, separately for the transitions to the "on" and "off" states according to the corresponding rates λ_k and $\bar{\lambda}_k$;
- The next event-related time step $\hat{t}_{next} = \min(\hat{t}_k)$ was therefore determined;
- All the potentials $v_0(t), \ldots, v_N(t)$ were integrated until $t = \hat{t}_{next}$, in steps of maximum $\delta_t = 10^{-5}$ s;
- Finally, the lamp states were updated.

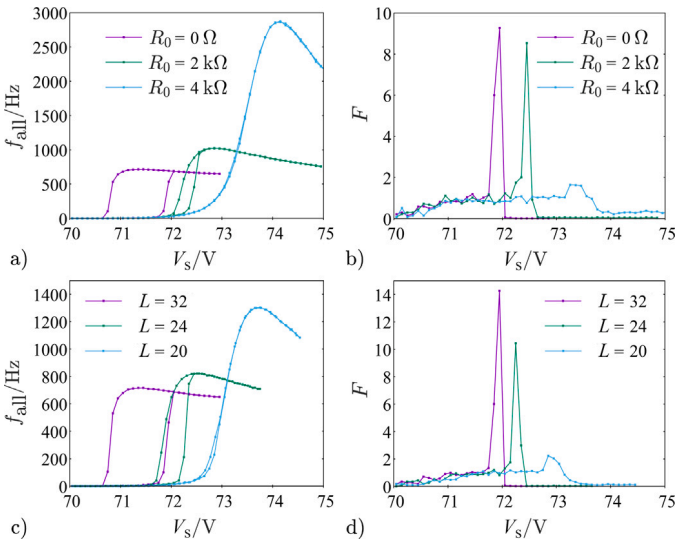

Fig. 8. Simulations of the array of neon lamps on the effect of the global series resistance R_0 and square array size L. (a) Overall event rate f_{all} as a function of the applied voltage V_s during hysteresis loops for different settings of R_0. (b) Corresponding Fano factor F (increasing voltage, averaging applied over 12 runs). (c) Overall event rate f_{all} as a function of the applied voltage V_s during closed loops for different settings of L. (d) Corresponding Fano factor F.

3.2. Hysteresis loops

A hysteresis loop of the supply voltage V_s was performed, starting from $V_s = 70$ V and reaching $V_s = 75$ V in 50 s (0.1 V/s), then returning to the starting value over the same amount of time, while recording for each time bin of $\delta_{bin} = 0.1$ s the event count, defined as the number of instantaneous transitions from the "off" to the "on" state. Groups of 10 consecutive time bins were thereafter pooled for calculating the average and variance of the event counts, in turn yielding the instantaneous rate, plotted in Fig. 8a. For $R_0 = 0\ \Omega$, the model showed a pronounced hysteresis effect, with $v_{up} = 71.9$ V and $v_{down} = 70.8$ V, corresponding to a hysteresis in the effect of the control voltage of $\Delta V_s = 1.1$ V. Increasing the value of R_0 reduced and eventually suppressed the hysteresis effect. For $R_0 = 2$ kΩ, $v_{up} = 72.4$ V and $v_{down} = 72.2$ V, yielding $\Delta V_s = 0.2$ V. For $R_0 = 4$ kΩ, the hysteresis was no longer appreciable. While these results replicate the main features of the physical measurements, an important discrepancy was found in that the maximum rate, rather than decreasing, increased with the resistance value, namely, $f_{all} = \{710, 1020, 2800\}$ Hz for the three values under consideration, hinting at some limitation of the model.

As in the experimental case, the question whether the vanishing of the discontinuous transition is marked by the presence of a critical point arises. To make a first attempt at addressing it, the Fano factor F, introduced in Eq. (1), is plotted in Fig. 8b (only over the first 50 s during which the supply voltage increases, as in Fig. 3b). As discussed in Section 2, it is expected that in presence of a critical point the Fano factor exhibits a peak, diverging with the size of the system, but no sign of such a divergence was observed [21,45–47]. More trivially, the peaks shown in Fig. 8b for $R_0 = 0$ Ω and 4 kΩ reflect the sharp discontinuity observed in the rate (i.e., transition during the observation window), but neither the large fluctuations that would produce a broader peak nor a maximum as a function of R_0 were observed. As shown below, this was due to the substantial autocorrelation time of the system in the vicinity of the critical point. Consequently, to successfully measure an increase of the Fano factor, it is necessary to average the event count and its fluctuations over very long time bins, on the order of tens of seconds. It is important to underline that this is fundamentally different

from the situation of the avalanche precursors observed as the spinodal line is approached [39]. Observing the increase in Fano factor in the vicinity of the critical point is only possible under an extremely slow change of the external potential or while measuring the fluctuations in the stationary state.

Finally, the influence of the array size L can be addressed, similarly as done for the experimental system, but considering a square array of size $N = L^2$. As said, for $L = 32$, the model showed a clear hysteresis effect, with $v_{up} = 71.9$ V and $v_{down} = 70.8$ V, corresponding to a hysteresis in the effect of the control voltage of $\Delta V_s = 1.1$ V. Decreasing the value of L reduced and eventually suppressed the hysteresis effect. For $L = 24$, $v_{up} = 72.3$ V and $v_{down} = 71.8$ V, yielding $\Delta V_s = 0.5$ V. For $L = 20$, the hysteresis was no longer appreciable. In other words, while the influence of the resistor value R_0 was, on the whole, similar to the experimental observations, the effect of the system size was different; for brevity, elucidating this discrepancy is left for future work, but it appears plausibly related to the fact that in the experimental system V_{on} and V_{off} were far from homogeneous, therefore embedding a form of "frozen variance", and may additionally have been influenced by memory effects [41]. In fact, insofar as the voltage fluctuations introduced in the array by individual events were concerned, also in the experimental system the effects of the resistor value R_0 and of the system size L were closely similar (Fig. 6b vs. 6c).

3.3. Static averages and critical point

In Fig. 9a, the region of the plane given by the parameters R_0 and V_s over which the system displays bistability is shown. For each setting of R_0 and V_s, it is expected that one of the two states will be preferred statistically when the dynamics are stationary. Therefore, by considering slower and slower hysteresis loops, the bistability region should shrink, in virtue of the fact that the system transitions earlier to the more stable state. In the limit of static averages, the region collapses into a line of discontinuous transition [47].

The first question to consider is, again, whether this line ends with a critical point, that is, a point where the correlations and fluctuations of the system diverge. To finally address this question in an appropriate setting, the system dynamics were simulated at a fixed value of the external potential. Let us first consider the autocorrelation time of the rate, which is determined based on the integral of the normalized autocorrelation function. The simulation can be segmented into time bins having a width of $\delta_{bin} = 100$ ms, and the rate $\rho(t)$ can be measured as the event count divided by δ_{bin}. One can then calculate

$$C(t) = \frac{\langle \rho(t')\rho(t'+t)\rangle - \langle \rho(t')\rangle^2}{\langle \rho(t')^2\rangle - \langle \rho(t')\rangle^2}, \tag{6}$$

where the average $\langle \cdots \rangle$ is determined on the running time t'. The function $C(t)$ starts from $C(0) = 1$ and decays to zero for long times. As shown in Fig. 9b, the time needed to decay to zero is maximized at the point where the two curves marking the limits of the bistability region meet, hinting at the presence of a critical point.

The Fano factor of the event count, introduced in Eq. (1), can be considered next, bearing in mind that it is strictly connected with the integral autocorrelation time of the rate. As previously indicated, if the number of events is extracted from a Poissonian distribution $P(n) = \frac{\mu^n}{n!}e^{-\mu}$, where $\mu = \rho(t)\delta_{bin}$ and $\rho(t)$ is constant over time, then the $F = 1$. If, however, $\rho(t)$ changes with an autocorrelation time τ_ρ, then for $\delta_{bin} \gg \tau_\rho$ one instead has

$$F = \langle \rho(t)\rangle^{-1} \int_{-\infty}^{\infty} \left[\langle \rho(t)\rho(t+t')\rangle - \langle \rho(t)\rangle^2\right] \, \mathrm{d}t'. \tag{7}$$

where, the process being assumed stationary, the average $\langle \cdots \rangle$ is independent of t. Therefore, in the presence of overdispersed dynamics, increasing the time bin δ_{bin}, one observes an increase of the Fano factor, until it reaches an asymptotic value given by Eq. (7) [21,45–47].

For the system under consideration, the largest autocorrelation time observed was about 10 s, so that the Fano factor would be expected to reach the asymptotic value for $\delta_{bin} \geq 10$ s. In Fig. 9c, the Fano factor computed over a bin width $\delta_{bin} = 25$ s is charted as a function of V_s and R_0. A sharp peak can be seen around $V_s = 72.5$ V and $R_0 = 2.5$ kΩ; this corresponds to the point where the two lines of Fig. 9a meet, with the small discrepancy being due to finite-time effects. It can therefore be concluded that the line of first-order transition ends with a *bona fide* critical point, where both the autocorrelation time and the Fano factor of the rate diverge. This explicitly shows that increasing the value of the global series resistance R_0 leads to a change from a first- to a second-order phase transition.

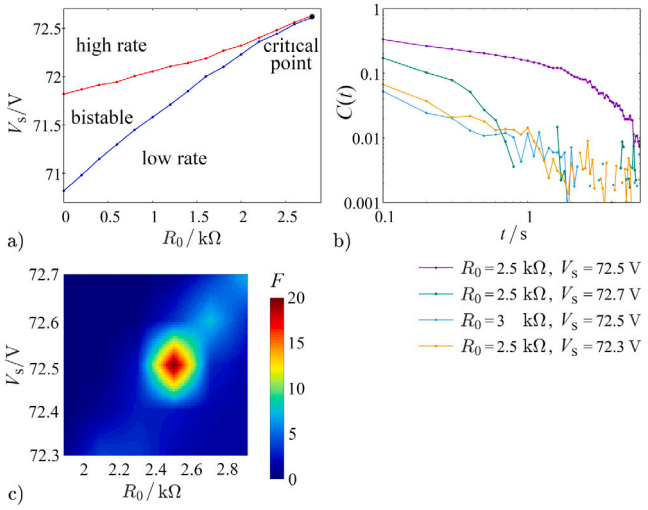

Fig. 9. Simulations under static V_s voltage conditions. (a) Phase diagram of the model: the red and blue lines denote, respectively, the upper and lower pseudo-spinodals, between which a region of bistability is found. (b) Autocorrelation decay of the event rate for different values of R_0 and V_s. The slowest decay (longest autocorrelation time) is found at the critical point. (c) Fano factor of the number of events as a function of the global series resistance R_0 and the supply voltage V_s. The peak at the value $R_0 \approx 2.5$ kΩ, $V_s \approx 72.5$ V corresponds to the critical point. (For interpretation of the references to color in this figure legend, the reader is referred to the web version of this article.)

The second question pertains to the mechanism by means of which the increase in the global series resistance R_0 eventually suppresses the discontinuous transition, that can be probed through considering several quantities measured at fixed values of the supply voltage V_s. Towards this end, simulations lasting until $t_{max} = 200$–500 s were performed, discarding the first 30 s to 200 s for to ensure thermalization (depending on the average rate, it takes between 2 and 16 min of CPU time to simulate 1 s of the dynamics using optimized code written in C language). The average event rate is charted in Fig. 10a, and it can be seen that it rapidly grows with the supply voltage V_s until it reaches a maximum where a plateau, or even a slow decrease, begins. The height of the plateau depends strongly on the global series resistance R_0, increasing sharply as its value becomes larger than 2 kΩ.

This unexpected behavior of the model can be explained by considering the average fraction of time during which at least one lamp is in the "on" state, referred to as f_{on} (not to be confused with a frequency), as shown in Fig. 10b. It can be seen that, for sufficiently small values of R_0, the interval over which the rate grows corresponds to $f_{on} \approx 0$, while the phase in which the rate remains constant or decreases corresponds to $f_{on} \approx 1$. Indeed, the overall event rate is controlled by the slowest between the rate of switching "on" and the rate of switching "off" of the lamps. When f_{on} is near zero (one), the switching "on" ("off") rate is the slowest one. In the first case, the rate increases with the external potential, while in the second it decreases, because the switching-off rate decreases with the potential across the lamp.

Another important aspect to consider is the mean and variance of the lamp potentials, charted in Fig. 10c. In the phase characterized by

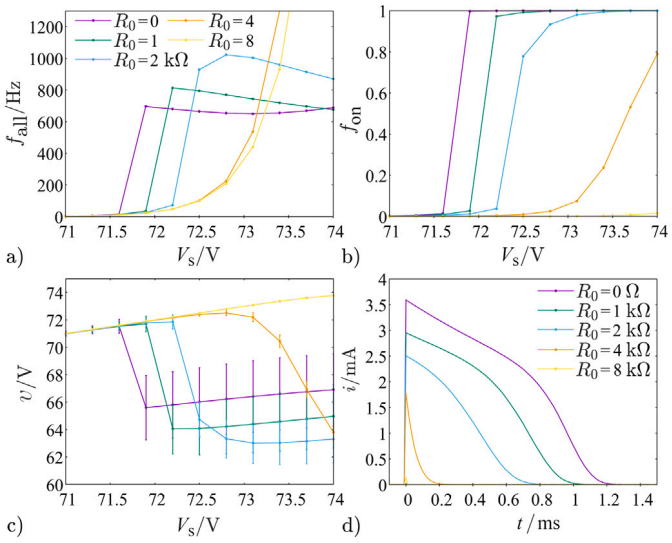

Fig. 10. Additional analyses on the simulated array of neon lamps. (a) Average event rate as a function of the supply voltage V_s for different values of R_0. (b) Fraction of time during which a lamp is in the "on" state. (c) Average and standard deviation of the lamp potentials. (d) Time-locked averaged current waveforms, for different values of R_0.

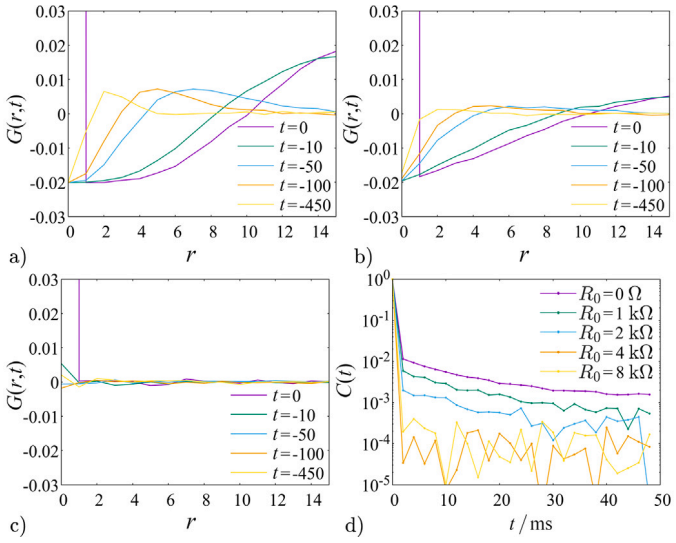

Fig. 11. Spatiotemporal correlations in the simulated array of neon lamps, given, (a) R_0 = 0 Ω, (b) R_0 = 2 kΩ, and (c) R_0 = 4 kΩ, respectively. The supply voltage was adjusted towards an average event rate per node of ≈14 Hz, yielding V_s = 71.6 V for (a), V_s = 71.7 V for (b) and (c). Time expressed in milliseconds. (d) Temporal correlations for the same R_0 and supply voltages.

$f_{on} \approx 0$, the mean potential is practically equal to V_s, and the variance is negligibly small. By contrast, when $f_{on} \approx 1$, the mean potential drops below V_s, by a voltage that grows with R_0, ranging from ≈5 V for R_0 = 0 Ω to ≈10 V for R_0 = 2 kΩ, while the variance grows. This effect is also directly connected with the fraction of time f_{on} that a lamp dwells in the "on" state. It has to be considered that, when a lamp is in the "off" state, the current flowing through the resistance R has the result of making the potential $v_k(t)$ relax towards that of the global node $v_0(t)$; conversely, while when a lamp is "on", this effect is largely counteracted by the current flowing through the lamp, that pulls the value of $v_k(t)$ towards the "ground" potential F. As a result, during the intervals of time while all the lamps are in the "off" state, the variance of the potentials v_k is reduced, whereas when one or more of the lamps are "on", the variance grows. Therefore, when $f_{on} \approx 0$, the variance is nearly zero, while for $f_{on} \approx 1$, it grows until it reaches a dynamical equilibrium, determined by the fact that the lamps with the highest potential are more like to transition to the "on" state, therefore, their potential tends to decrease.

The last ingredient to consider is the reason why the global resistance has the effect of pushing forward the potential at which the system enters the phase with $f_{on} \approx 1$ as also visible, albeit less markedly, for the experimental recordings in Fig. 3b. This is connected with the duration of the "on" state, which can be assessed by charting the shape of the current flowing through the circuit after the switching "on" of a lamp, as shown in Fig. 10d. For low values of R_0, the potential reached by the lamps that switch "on" is relatively high: consequently, the lamp remains for a long time in the "on" state, giving time for the variance of the potentials to increase. On the other hand, when R_0 is large, the potential reached by the lamp is lower, therefore, the time that it remains in the "on" state is shorter, and the variance of the potentials remains contained. As shown in Fig. 6b, also this effect was clearly visible in the experimental recordings. Therefore, for increasing R_0, the systems preferentially dwells in the state with low variance and $f_{on} \approx 0$ over a large span of supply voltages V_s.

3.4. Spatio-temporal correlations

The amount of time that a lamp spends in the "on" state has important consequences also for the spatiotemporal correlations in the system. When a lamp fires, that is, generates an event by switching "on", its potential becomes lower than the average, therefore, the probability that it fires again shortly afterwards is low, realizing a sort of refractoriness. It is noteworthy that refractoriness, a fundamental property of biological neurons, here emerges spontaneously as a function of the dynamics of the voltages in the array [1]. This can be appreciated in Fig. 11a–c, assuming the system is sufficiently isotropic and charting the correlation $G(r,t)$, that is given by

$$G(\boldsymbol{r},t) = \langle \rho(\boldsymbol{r}'+\boldsymbol{r},t'+t)\rho(\boldsymbol{r}',t')\rangle - \langle \rho(\boldsymbol{r}',t')\rangle^2, \tag{8}$$

where $\rho(\boldsymbol{r}',t')$ is the rate at position $\boldsymbol{r}'$ and time t', and the average $\langle\cdots\rangle$ is done on the position $\boldsymbol{r}'$ and the times t'. As in the case of temporal correlations, rates are computed over time bins of width δ_{bin} = 100 ms. This correlation measures the excess probability (with respect to the mean value) that a lamp fires at time t and distance r from the origin, given that a lamp has fired in the origin at time 0. This probability tends to be lower near the origin, and becomes flat only when the time separation is sufficiently large. However, for large values of R_0, this effect is suppressed, so that the correlations drop practically to zero for R_0 = 8 kΩ. This effect is due to the average time that a lamp dwells in the "on" state, which is lower for higher values of R_0, as can be seen from Fig. 10d; consequently, the potential of the lamp has less time to deviate from the average. The same effect can be seen in the temporal correlations $C(t) = 2\pi \int rG(r,t)\,\mathrm{d}r$, charted in Fig. 11d, that is, the excess probability that a lamp fires at time t, given that a lamp has fired at time 0, which becomes practically zero as the global series resistance R_0 increases. In other words, the effect of increasing R_0 was primarily to dissolve the finite-range spatiotemporal correlations initially present in the bistability region, while at the same time their spatial integral is maximized at the critical point.

3.5. Model with adjusted parameter settings

Given the model parameter settings considered thus far, the event rate reaches a maximum when increasing the external potential then starts decreasing, as can be seen in Fig. 8, due to the fact that when $f_{on} \approx 1$ the rate is controlled to the switching "off" of the lamp, and this decreases with the potential according to $\rho_{off} \exp\left(\frac{V_{off}-v_k(t)}{D_{off}}\right)$. In the experimental system, this behavior was not observed. If the value of

D_{off} is increased compared to the initial setting from Ref. [39], which merely represents an arbitrary choice, the switching "off" rate depends less on the potential of the lamp, and one can expect that this will, in turn, prevent the decrease of the rate upon increasing the external potential.

A modified model was therefore considered, setting $D_{\text{off}} = 25$ V instead of $D_{\text{off}} = 0.4$ V. Moreover, to make the order of magnitude of the rate more similar to the experimental one, the capacitances were increased and the rates were decreased, setting $C_{ij} = 1.3$ μF, $\rho_{\text{on}} = 0.167$ ms^{-1}, and $\rho_{\text{off}} = 0.333$ ms^{-1}. The rate during a hysteresis plot is shown in Fig. 12a, and is closer to the experimental results, see Fig. 3. In Fig. 12b,c and d, the spatiotemporal and temporal correlations are charted as a function of the global series resistance R_0, showing the same decrease with R_0 as observed with the initial parameter settings, thus reassuring about the generality of the findings.

3.6. Commentary

To summarize, these simulations using an extended numerical model of the array of neon lamps first of all confirmed that the effect of the additional global resistor was not due to a non-ideality of the experimental apparatus. The observations could be largely replicated through an event-driven simulation, integrating the continuous evolution of the potentials over the array of capacitors in between stochastic flashing events, which were generated according to simple exponential voltage-dependent rates. Notably, these simulations also confirmed that the effect was observable under the assumption of identical nodes. Furthermore, thanks to the ability to perform simulations over long time-periods under static conditions, it was possible to observe that there is an extended region of bistability which, as a function of both the supply voltage and the global series resistor, eventually shrinks into the critical point. Therefore, it was proven that the additional resistor can lead to a shift from first- to second-order transition in the system dynamics. These simulations also revealed that the requirements for observing the divergence of the Fano factor are fundamentally different between the situation where the spinodal line is approached and transition precursors are observed, and the situation where the true critical point of the system is approached: in the latter case, the autocorrelation time becomes very long, posing demanding requirements on the bin size which hindered experimental measurement. No less importantly, it was possible to precisely explain why the additional resistor exerts the observed influence on the transition order. The effect could eventually be ascribed to the average fraction of time that a lamp spends in the "on" state, which directly impacts the amount of variance that is generated. For increasing resistance values, the spatiotemporal correlations initially characterizing the dynamics in the bistability region are quickly washed out, only to reappear and diverge in the vicinity of the critical point.

4. A mean-field approximation

4.1. Model formulation

Having demonstrated experimentally and through an extended numerical model the effect of the global series resistance R_0, a mean-field model that recapitulates the behavior of the system shall now be introduced. As further detailed in Section 5, this serves particularly as a stepping stone towards neural mass models, such as the Wilson–Cowan model. Let us consider a set of N units (lamps), having potentials $v_k(t)$ at a time t, with $k = 1, \ldots, N$, and let $m(t)$ be the instantaneous value of the spatial standard deviation across the node potentials, namely

$$m(t) = \sqrt{\langle v_k(t)^2 \rangle - \langle v_k(t) \rangle^2}, \tag{9}$$

where $\langle \cdots \rangle$ denotes the average over the N lamps at time t. Denoting with $\rho(t)\delta t$ the probability that an event (transition of a lamp to the "on" state) takes place during the time interval $[t, t+\delta t]$, as a first-order

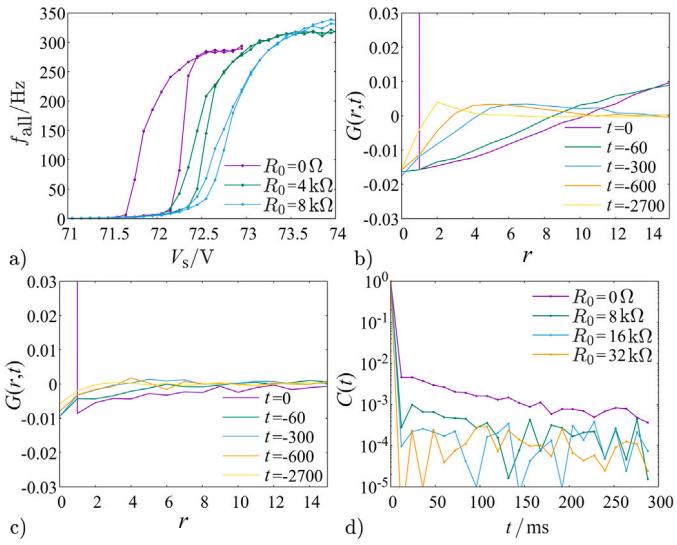

Fig. 12. Additional analyses on the simulated array of neon lamps with adjusted parameters. (a) Average event rate as a function of the supply voltage V_s for different values of R_0. (b,c) Spatiotemporal correlations for $R_0 = 0$ Ω and $R_0 = 32$ kΩ, respectively. The supply voltage was adjusted towards an average event rate per node of ≈ 2.3 Hz, yielding $V_s = 71.65$ V for (a), $V_s = 71.7$ V for (b) and (c) Time expressed in milliseconds. (d) Temporal correlations for the same R_0 and supply voltages.

approximation one can assume that the instantaneous rate $\rho(t)$ (not to be confused with the transition rates ρ_{on} and ρ_{off} in the Section 3) is given by

$$\rho(t) = f\left(V_s + m(t)\right), \tag{10}$$

where V_s denotes the external supply voltage applied to the system through R_0 as shown in Fig. 1a, and $f(v) \geq 0$ represents an activation function. The rationale of Eq. (10) is that the overall rate is, to a large extent, determined by the lamps that experience the largest voltage, which is, in turn, on the order of the mean plus the standard deviation. Here, the mean voltage is assumed to be V_s, which is true when all the lamps are in the "off" state. Also, based on the results from the extended model in Section 3, the probability that two lamps are in the "on" state at the same time is being neglected, so that an event can be generated only when all the lamps are off and the mean value of the potentials is V_s.

Furthermore, let us assume that each event makes the standard deviation $m(t)$ grow by a fixed "quantum" ϵ, and that $m(t)$ relaxes back to zero exponentially with a characteristic time τ, giving

$$m(t) = \epsilon \int_{-\infty}^{t} e^{-(t-t')/\tau} \sum_k \delta(t' - t_k) \mathrm{d}t' = \epsilon \sum_k e^{-(t-t_k)/\tau}, \tag{11}$$

where t_k are the event times, and $\delta(x)$ is Dirac's delta function. Under quasi-stationary conditions, that is when $\rho(t) \approx \rho^*$, and assuming that $\rho^* \tau \gg 1$, the standard deviation shall fluctuate with $m(t) \approx m^* = \tau \epsilon \rho^*$, leading to the self-consistent equation

$$\rho^* = f(V_s + \tau \epsilon \rho^*). \tag{12}$$

The solutions ρ^*, that is, the fixed points of Eq. (12), correspond the possible stationary states of the system.

It follows that the shape of $f(v)$ is of paramount importance because it determines whether the system can have simultaneously more than one fixed point or not. Accordingly, it needs to feature a change of convexity at some value of the argument, so that the first derivative is not monotone. Indeed, the solutions of Eq. (12) correspond to zeros of the function $F(\rho) = f(V_s + \tau \epsilon \rho) - \rho$ (not to be confused with the Fano factor F). As will be shown in the next subsection, if at the solution $F'(\rho) < 0$, the fixed point is stable in the sense that the

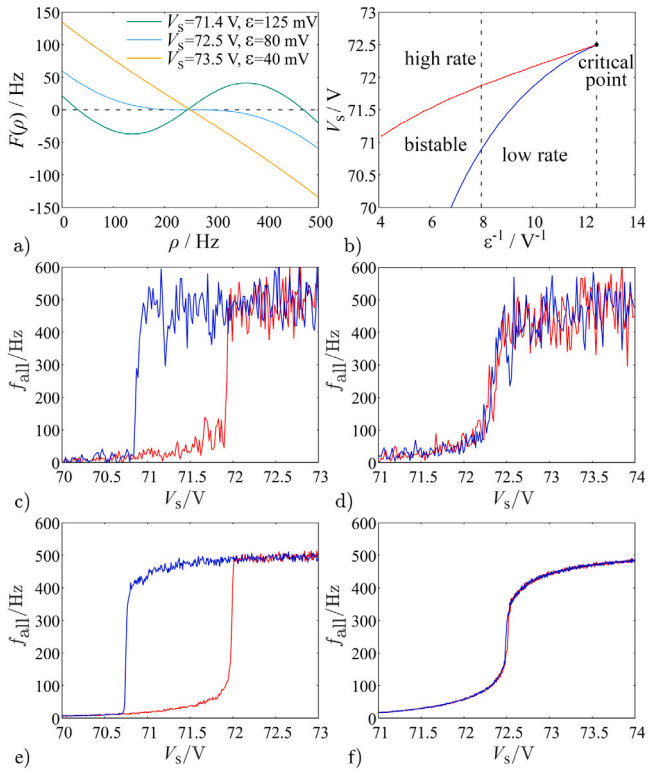

Fig. 13. Calculations based on the mean-field model. (a) The function $f(v)$ for different values of V_s and ϵ. (b) Region in the plane of ϵ and V_s where two stable fixed points exist. The red and blue lines denote, respectively, the upper and lower spinodal, between which a region of bistability is found. The dashed lines represent the values corresponding to the hysteresis loops in panels c and d. (c) and (d) Hysteresis loops for $\epsilon = 125$ mV and $\epsilon = 80$ mV (critical value), respectively. (e) and (f) Corresponding Hysteresis loops for $\tau = 10$ s, $\epsilon = 1.25$ mV and $\epsilon = 0.8$ mV (critical value), respectively. (For interpretation of the references to color in this figure legend, the reader is referred to the web version of this article.)

dynamics fluctuate around the fixed point, whereas the solutions with $F'(\rho) > 0$ correspond to unstable fixed points. To exhibit two stable fixed points, the function $F(\rho)$ has to cross the ρ-axis twice with a negative derivative.

Without loss of generality, let us consider the activation function

$$f(v) = \beta \left[1 + \exp\left(\frac{V_{on} - v}{D_{on}}\right)\right]^{-1}. \quad (13)$$

For $v < V_{on}$, it is similar to that considered throughout Section 3, while for $v > V_{on}$ it saturates, taking into account the finite time needed for a lamp to switch off, as the model otherwise represents lamp flashings purely like a point process. Let us consider the following parameter settings: event rate scale $\beta = 500$ Hz (implicitly corresponding to the system size), characteristic time $\tau = 100$ ms, characteristic breakdown voltage $V_{on} = 74.5$ V, and corresponding scaling coefficient $D_{on} = 1$ V.

In Fig. 13a, the function $F(\rho)$ is charted as a function of ρ, for different values of V_s and ϵ. The critical point is obtained when it crosses the ρ-axis with a derivative equal to zero. In this case, the fixed point is only marginally stable, and large fluctuations occur, as shown in the next subsection. With the parameter settings considered, this happens for $V_s = 72.5$ V, $\epsilon = 0.08$ V, shown as the red curve in Fig. 13a. It is important to note that, for larger values of ϵ, the function can have two stable fixed points within a certain interval of V_s. Conversely, for smaller values of ϵ, it always has a single stable fixed point. In Fig. 13b, the region of the parameters V_s and ϵ wherein two stable fixed points exist is shown. The critical point corresponds to the point where the two lines meet.

It is therefore clear that the parameter ϵ^{-1} plays a role similar to the global series resistance R_0 in the extended model. Accordingly, when the value of ϵ is lowered, the variance of the potentials decreases, giving rise to the same effect that an increase in R_0 exerts on the original model through reducing the time that the lamps remain in the "on" state.

4.2. Numerical results

The approach used in the previous section is based only on the analysis of the fixed points of Eq. (12), neglecting the fluctuations of $\rho(t)$ and $m(t)$ around the fixed point values ρ^* and m^*. This is correct as long as the product $\rho^*\tau$ tends to infinite, which can be achieved in two ways: sending τ to infinity with $\tau\epsilon$ held fixed (so that ρ^* and m^* remain the same), or sending β to infinity with the product $\beta\epsilon$ held fixed (so that ρ^*/β and m^* remain the same). However, in practice, $\rho^*\tau$ is finite, leading to fluctuations of $\rho(t)$ and $m(t)$. Moving beyond this initial approximation, it will now be shown that the variance and autocorrelation of the fluctuations can be derived analytically, as done in the following subsection, or computed making an explicit simulation of the model, that is, generating a sequence of spikes by means of the following procedure.

One starts with $k = 0$ and $t_0 = 0$, given an initial standard deviation $m(t_0) = 0$, and iterates the following steps:

- Compute the instantaneous rate $\rho(t_k)$ from Eq. (10);
- Randomly extract the time $t_{k+1} = t_k + \Delta t_k$ of the next event from the inter-event time distribution $p(\Delta t_k) \propto e^{-\rho(t_k)\Delta t_k}$ representing a Poissonian process;
- Compute the standard deviation before the spike $m(t_{k+1}^-) = m(t_k)\, e^{-\Delta t_k/\tau}$;
- Generate the spike at time t_{k+1} and then compute the standard deviation after it, $m(t_{k+1}^+) = m(t_{k+1}^-) + \epsilon$;
- Finally, update $k \to k + 1$.

Note that at the second step the rate $\rho(t)$ is assumed constant over the time interval $[t_k, t_{k+1})$. This approximation could be overcome by using a more refined algorithm, however it is adequate insofar as the flashing rate is greater than τ^{-1}.

Fig. 13c and d depict the event rate during a hysteresis loop in the course of which the potential is increased from $V_s = 70$ to 74 V over 50 s, and then decreased back to 74 V over the same amount of time. The rate was computed in time bins with $\delta_{bin} = 0.2$ s. Specifically, Fig. 13c is for $\tau = 100$ ms and $\epsilon = 125$ mV (corresponding to the left dashed line in Fig. 13b), while Fig. 13d is for $\epsilon = 80$ mV (corresponding to the right dashed line in Fig. 13b, passing through the critical point). In the former case, a clear hysteresis effect could be seen, with $v_{up} = 71.9$ V and $v_{down} = 70.9$ V, corresponding to a hysteresis in the effect of the control voltage of $\Delta V_s = 1.0$ V. Decreasing the value of ϵ shrank, and eventually suppressed, the hysteresis effect. As shown in Fig. 13e and f, decreasing the "quantum" of variance ϵ and elongating the time-scale τ by a factor of 100 considerably reduced the residual fluctuations, leaving the effect otherwise essentially unaltered.

4.3. Analytical determination of the fluctuations

To derive the fixed point equations, thus far the term $\sum_k \delta(t' - t_k)$ appearing in Eq. (11) was approximated as the mean rate ρ^*. A less crude approximation is given by

$$\sum_k \delta(t' - t_k) \simeq \rho(t) + \sqrt{\rho^*}\,\eta(t), \quad (14)$$

where $\eta(t)$ represents a Gaussian noise characterized by $\langle\eta(t)\rangle = 0$, $\langle\eta(t)\eta(t')\rangle = \delta(t - t')$. Entering this into Eq. (11), and deriving with respect to time, one obtains

$$\dot{m}(t) = -\frac{1}{\tau}m(t) + \epsilon\rho(t) + \epsilon\sqrt{\rho^*}\,\eta(t). \quad (15)$$

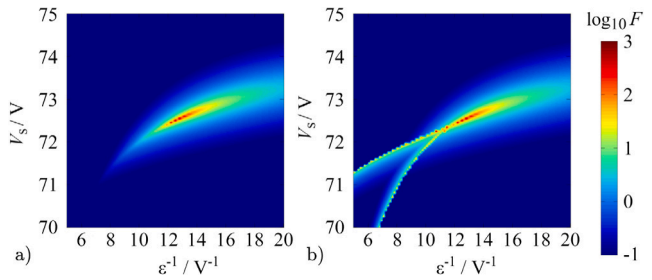

Fig. 14. Parametric maps of the Fano factor, calculated from the mean-field model, as a function of ϵ^{-1} and V_s. (a) Minimum and (b) Maximum value.

At stationarity, the rate $\rho(t)$ and the standard deviation $m(t)$ fluctuate around the fixed point values ρ^* and m^*, where ρ^* is a solution of Eq. (12), and $m^* = \epsilon\tau\rho^*$. Defining $\delta m(t) = m(t) - m^*$, from Eq. (10), one has

$$\rho(t) \simeq \rho^* + f'(V_s + m^*)\,\delta m(t). \tag{16}$$

It follows that

$$\dot{m}(t) = -\lambda\,\delta m(t) + \epsilon\sqrt{\rho^*}\eta(t), \tag{17}$$

where

$$\lambda = \tau^{-1} - \epsilon f'(V_s + m^*) = -\tau^{-1}F'(\rho^*). \tag{18}$$

From this equation, it is clear that the attractive fixed points are characterized by $\lambda > 0$, that is, by $F'(\rho^*) < 0$, as previously mentioned. The parameter λ^{-1} represents the relaxation time of the fluctuations in $\rho(t)$ and $m(t)$, and was previously undefined under the assumption of constant m. It diverges in $\lambda^{-1} \to \infty$ at the critical point, where $F'(\rho^*) = 0$. The critical fixed point is attractive only marginally, that is, considering successive derivatives of $F(\rho)$.

From Eq. (17), one can compute the autocorrelation of the fluctuations, given by

$$\langle \delta m(t)\delta m(t')\rangle = \frac{\epsilon^2\rho^*}{2\lambda}e^{-\lambda|t-t'|}. \tag{19}$$

Considering an interval of time $[t, t+\Delta t]$, the number of events taking place within the interval is given by

$$\begin{aligned} n_{\text{events}} &= \int_t^{t+\Delta t} \rho(t')\,\mathrm{d}t' \\ &= \rho^*\Delta t + \epsilon^{-1}\left(\tau^{-1} - \lambda\right)\int_t^{t+\Delta t} \delta m(t')\,\mathrm{d}t', \end{aligned} \tag{20}$$

where Eqs. (16) and (18) were imported. The Fano factor then is given by Eqs. (1) and (7), where it is assumed that Δt is greater than the autocorrelation time of $\rho(t)$. Using Eqs. (16), (18) and (19), finally one obtains

$$F = \left(\frac{1}{\lambda\tau} - 1\right)^2, \tag{21}$$

where, as said, the time τ denotes the relatively fast decay of $m(t)$ towards zero and λ^{-1} is the characteristic time of the slower fluctuations which diverge at the critical point.

In Fig. 14a and b that correspond, respectively, to the minimum (more stable) and maximum Fano factor, the same is shown as a function of ϵ^{-1} and V_s, focusing on the region of bistability around the two fixed points. The divergence at the critical point, $\epsilon^{-1} = 12.5$ V^{-1}, $V_s = 72.5$ V, is well evident, and the line of maxima starting at the critical point and going in the up right direction can be appreciated. This corresponds to the Widom line, which in phase diagrams originates from the critical point and rises in the supercritical region, defined as the locus of maxima of the correlation length or of the fluctuations, separating a "liquid-like" from a "gas-like" behavior [47]. In Fig. 14b, the spinodal lines, that is the lines where one of the solutions becomes unstable and the fluctuations diverge, are also visible. The corresponding solutions of the equation $F(\rho) = 0$ are characterized by the fact that the function touches the ρ-axis not at an horizontal inflection point, as for the critical point, but at a minimum or a maximum.

4.4. Commentary

Some important conclusions can be drawn from this model. The first is that the critical point always exists at the end of the lines delineating the region of bistability, and its location corresponds to a pair of values for the global series resistance R_0 and applied voltage V_s. The second is that the shape of the activation function plays a central role in determining the order of the transition. The third is that the presence and width of the bistability and hysteresis are directly determined by the "quantum" of variance that each event introduces in the system, to be considered in proportion with respect to the relaxation time scale. The fourth is that the effect is quite general, and could therefore be observed across diverse scenarios that can be in one way or another reconduced to this abstract model.

5. Micro- and mesoscopic neural dynamics

5.1. Wilson-Cowan model

The mean-field approximation described in Section 4 has aspects of similarity with several well-known models of neural activity, especially the so-called neural mass models. These models represent entire neuron populations in an aggregate form through a small number of state variables corresponding, for instance, to the level of activity in the excitatory and inhibitory subpopulations. They are, therefore, abstracted from the spatiotemporal evolution of the membrane potentials in the same way that the proposed mean-field approximation is from the potentials in the neon lamp array. One of the most established neural mass models is the Wilson–Cowan model [49,50].

According to it, neural activity is characterized by two neuron populations, one excitatory and the other inhibitory. Each unit (neuron) can be in the "on" or "off" state, as represented by a binary variable $a_i = 0, 1$, and remains in the active state after spiking for a time determined by a constant extinction rate akin to the parameter τ in Section 4. By contrast, the activation rate is a function of the number of afferent neurons that are in the "on" state. In other words, an active neuron spontaneously becomes quiescent according to an extinction rate α, while a quiescent one becomes active according to an activation rate $f(s_i)$, where

$$s_i = \sum_j w_{ij}a_j + h_i \tag{22}$$

is the input of the ith neuron. The parameters w_{ij} represent the strengths of the connections between pre-synaptic neuron j and post-synaptic neuron i, and h_i the external input to neuron i. The function $f(s)$ is akin to $f(v)$ defined in Section 4: while $f(v)$ represents the flashing rate of a lamp subject to a potential v, here $f(s)$ is the spiking rate of a neuron whose synaptic input is s.

In the simplest formulation of the model, neurons are wired up in an all-to-all topology with identical connections, depending only on the nature (excitatory or inhibitory) of the neurons. This tantamounts to a mean-field configuration, where the input of a neuron depends only on two variables, namely, the fractions f_E and f_I of active excitatory and inhibitory neurons. The weights of the corresponding outgoing connections are typically normalized to w_E/N_E and w_I/N_I, where N_E and N_I denote, respectively, the two subpopulation sizes. One can write

$$s = w_E f_E - w_I f_I + h, \tag{23}$$

where h is the external input, assumed to be equal across all the neurons. In the following, we also assume that $N_E = N_I = N$. In the Van

Kampen's system-size expansion [51] the fractions of active neurons obey the equations

$$\begin{cases} \dfrac{\mathrm{d}f_\mathrm{E}}{\mathrm{d}t} = -\alpha f_\mathrm{E} + (1-f_\mathrm{E})f(s) \\ \qquad + N^{-1/2}\sqrt{\alpha f_\mathrm{E} + (1-f_\mathrm{E})f(s)}\,\eta_\mathrm{E}(t) \\ \dfrac{\mathrm{d}f_\mathrm{I}}{\mathrm{d}t} = -\alpha f_\mathrm{I} + (1-f_\mathrm{I})f(s) \\ \qquad + N^{-1/2}\sqrt{\alpha f_\mathrm{I} + (1-f_\mathrm{I})f(s)}\,\eta_\mathrm{I}(t), \end{cases} \tag{24}$$

where $\eta_\mathrm{E}(t)$ and $\eta_\mathrm{I}(t)$ are independent Gaussian white noises, with $\langle\eta_x(t)\rangle = 0$ and $\langle\eta_x(t)\eta_y(t')\rangle = \delta_{x,y}\delta(t-t')$.

Neglecting the stochastic terms in Eq. (24), and defining the total activity as $\Sigma = (f_\mathrm{E} + f_\mathrm{I})/2$ and the imbalance as $\Delta = (f_\mathrm{E} - f_\mathrm{I})/2$, one obtains the deterministic equations

$$\begin{cases} \dfrac{\mathrm{d}\Sigma}{\mathrm{d}t} = -\alpha\Sigma + (1-\Sigma)f(s), \\ \dfrac{\mathrm{d}\Delta}{\mathrm{d}t} = -[\alpha + f(s)]\,\Delta, \end{cases} \tag{25}$$

where $s = w_0\Sigma + w_s\Delta + h$, $w_0 = w_\mathrm{E} - w_\mathrm{I}$, and $w_s = w_\mathrm{E} + w_\mathrm{I}$. In this way, over sufficiently long times the total activity and the imbalance converge, apart from $N^{-1/2}$ fluctuations, to the fixed point (Σ^*, Δ^*), defined by $\Delta^* = 0$ and

$$\alpha\Sigma^* = (1-\Sigma^*)f(w_0\Sigma^* + h). \tag{26}$$

Similarly to the situation in Section 4, depending on the values of the parameters and the shape of the activation function $f(s)$, Eq. (26) can have one or two attractive solutions. Let us consider the activation function

$$f(s) = \frac{\beta}{1+\exp(\theta - s)}, \tag{27}$$

with the parameter settings $\alpha = \beta = 0.1$ ms^{-1}, $w_\mathrm{E} = 14$, and threshold $\theta = 6$. In Fig. 15a, the region of the plane (w_I, h) where two attractive solutions exist is shown. It can be seen that this region ends in the critical point, which, in this case, is given by $w_\mathrm{I} = 6$ and $h = 4 - \log 2 \approx 3.31$.

The model can be simulated by means of an algorithm similar to that described in Section 4. Let $N = 5000$, the number of active excitatory and inhibitory neurons is given, respectively, by $k = Nf_\mathrm{E}$ and $l = Nf_\mathrm{I}$. At a time t, the deactivation rate $\alpha(k+l)$ and the activation rate $\rho = (2N - k - l)f(s)$, where s is given by Eq. (23), are computed prior to the next event, and a neuron is activated or deactivated correspondingly. As shown in the previous cases, hysteresis loops can be performed at different intensities of global inhibition. In this case, the excitatory input h is the parameter that is varied, starting from $h = 0$ and increasing it up to $h = 6$, and then decreasing it back to $h = 0$, at different values of w_I. The functions of these two parameters largely correspond to the voltage V_s and resistance R_0 in Section 4. In Fig. 15b the flashing rate is charted as a function of h, and a clear hysteresis effect can be seen for $w_\mathrm{I} < 6$.

To compute the fluctuations of the event count in the vicinity of the fixed point of the dynamics, it is convenient to define $\Sigma = \Sigma^* + N^{-1/2}\xi_\Sigma$ and $\Delta = N^{-1/2}\xi_\Delta$. By making a Taylor expansion of $f(s)$ around the fixed point $s^* = w_0\Sigma^* + h$, one finds that terms of order N^0 vanish, while terms of order $N^{-1/2}$ give the equations [52–54]

$$\frac{\mathrm{d}}{\mathrm{d}t}\begin{pmatrix}\xi_\Sigma \\ \xi_\Delta\end{pmatrix} = \begin{pmatrix}-\tau_1^{-1} & w_\mathrm{FF} \\ 0 & -\tau_2^{-1}\end{pmatrix}\begin{pmatrix}\xi_\Sigma \\ \xi_\Delta\end{pmatrix} + \sqrt{2\alpha\Sigma^*}\begin{pmatrix}\eta_\Sigma(t) \\ \eta_\Delta(t)\end{pmatrix}, \tag{28}$$

where $\tau_1^{-1} = \alpha + f(s^*) - (1-\Sigma^*)w_0 f'(s^*)$ and $\tau_2^{-1} = \alpha + f(s^*)$ are the relaxation rates of the two eigenvectors, $w_\mathrm{FF} = (1-\Sigma^*)(w_\mathrm{E} + w_\mathrm{I})f'(s^*)$ is the feed-forward strength [49,50], and $\eta_\Sigma(t) = \frac{\eta_\mathrm{E}(t)+\eta_\mathrm{I}(t)}{\sqrt{2}}$ and $\eta_\Delta(t) = \frac{\eta_\mathrm{E}(t)-\eta_\mathrm{I}(t)}{\sqrt{2}}$ are uncorrelated white noises.

The correlation functions of the fluctuations $\xi_\Sigma(t)$ and $\xi_\Delta(t)$ can be derived analytically from the linear Langevin Eq. (28) [53,54]. The covariance matrix $\sigma_{ij} = \langle\xi_i(0)\xi_j(0)\rangle$ with $i,j = (\Sigma,\Delta)$, where $\langle\cdots\rangle$ denotes an average in the stationary state, satisfies the relation [55]

$$-\begin{pmatrix}\alpha\Sigma^* & 0 \\ 0 & \alpha\Sigma^*\end{pmatrix} = A\sigma + \sigma A^T, \tag{29}$$

where A is the matrix appearing in Eq. (28). While the detailed steps are omitted for brevity, the elements $C_{\Sigma\Sigma}(t)$, $C_{\Sigma\Delta}(t)$, $C_{\Delta\Sigma}(t)$, and $C_{\Delta\Delta}(t)$ of the time correlation matrix $C(t)$ can then be obtained from the equations [55]

$$C_{ij}(t) = (e^{At}\sigma)_{ij}. \tag{30}$$

Within the linear approximation valid in the limit of a large neuron number and the assumption of a stationary state, the deterministic components having relaxed to the attractive fixed point, the firing rate can be Taylor expanded around the fixed point, giving

$$\rho(t) = 2N\,(1-\Sigma(t))\,f\left(w_0\Sigma(t) + w_s\Delta(t) + h\right) \tag{31}$$

$$\simeq N\rho^* + N^{1/2}\xi_\rho(t), \tag{32}$$

where

$$\xi_\rho(t) = \left(\alpha - \tau_1^{-1}\right)\xi_\Sigma(t) + w_\mathrm{FF}\xi_\Delta(t). \tag{33}$$

The autocorrelation function of $\xi_\rho(t)$ can then be computed as

$$\langle\xi_\rho(t)\xi_\rho(0)\rangle = \left(\alpha - \tau_1^{-1}\right)^2 C_{\Sigma\Sigma}(t) + w_\mathrm{FF}\left(\alpha - \tau_1^{-1}\right)\left[C_{\Sigma\Delta}(t) + C_{\Delta\Sigma}(t)\right] + w_\mathrm{FF}^2 C_{\Delta\Delta}(t).$$

From these, using Eq. (7), the Fano factor can be computed as in Section 4, and the result is visible in Fig. 15c. In the region of bistability, the solution with the lowest Fano factor was taken. As expected, the Fano factor diverges at the critical point.

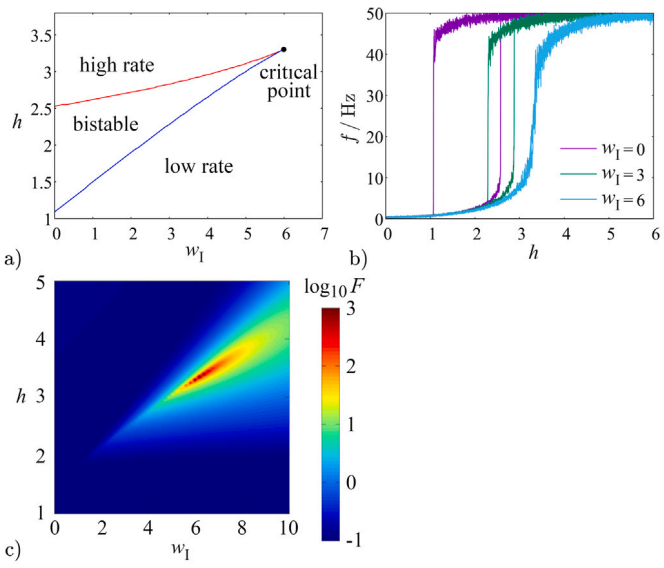

Fig. 15. Simulations of the Wilson–Cowan model. (a) Region of the plane (w_I, h) where two stable solutions exist, ending in the critical point. The red and blue lines denote, respectively, the upper and lower spinodal, between which a region of bistability is found. (b) Firing rate during an hysteresis loop of the external input, for different intensities of the global inhibition. (c) Fano factor as a function of the inhibition intensity w_I and the external input strength h. (For interpretation of the references to color in this figure legend, the reader is referred to the web version of this article.)

5.2. Leaky integrate-and-fire neurons

As a final step, it can be shown that the postulated effect of global inhibition also holds in a detailed model of neural dynamics that represents the full spatiotemporal evolution of the membrane potentials. A

model in widespread use is the leaky integrate-and-fire neuron, wherein the membrane potential is influenced by the integral of the inflowing current, that, in turn, depends upon the spiking of the afferent neurons [56,57]. In the deterministic version of the model, a neuron spikes whenever the potential reaches a given threshold value, whereas in the stochastic version, the spiking probability is a continuously growing function of the membrane potential, similarly as the neon lamps considered in Section 4. These related models show strikingly similar behaviors, whereby for low global inhibition they can display bistability and hysteresis as a function of the excitability, while for higher global inhibition the bistability region shrinks and ends with a critical point. This similarity was, in fact, *ab initio* one of the primary drivers for using neon lamps to construct the experimental system in Section 1. For even higher global inhibition the spiking rate becomes a smooth, continuous function of the excitability. In the following, these behaviors are demonstrated.

A leaky integrate-and-fire ith neuron is modeled as a simple parallel RC circuit, in which the potential obeys the equation

$$C_i \frac{\mathrm{d}V_i(t)}{\mathrm{d}t} = -\frac{V_i(t) - V_0}{R_i} + I_i(t), \tag{34}$$

where C_i is the membrane capacity, $\tau_m = R_i C_i$ is the membrane characteristic time, and V_0 the resting potential of the neuron. When the potential $V_i(t)$ reaches a threshold V_θ, the neuron fires (emits a spike) and the potential is reset to V_0. The input current, flowing through the dendrites, is given by

$$I_i(t) = \sum_{j \neq i} J_{ij} \sum_{t_i < t_j < t} e^{-(t-t_j)/\tau_s} + \sum_{\hat{t}_i} \kappa(\hat{t}_i) e^{-(\hat{t}_i - t_j)/\tau_s}. \tag{35}$$

The first term denotes the input current due to the spikings in other neurons of the network, linked to neuron i through synapses of strength J_{ij}, where t_j are the spike times of neuron j. The second term takes into account the input from other sources, such as neurons outside the network under consideration, and is modeled as a series of spikes occurring at random Poissonian-distributed times $\hat{t}_i$ with a strength $\kappa(\hat{t}_i)$. The values of J_{ij} or $\kappa(\hat{t}_i)$ represents the peaks of the input current, which decays exponentially with a synapse characteristic time τ_s.

Let us consider physiologically realistic parameter settings, such as $V_0 = -70$ mV, $V_\theta = -55$ mV, $C_i = 0.1$ nF, $R_i = 100$ MΩ, so that $\tau_m = C_i R_i = 10$ ms, and $\tau_s = 5$ ms [1]. The random Poissonian spikes $\hat{t}_i$ are extracted with a rate of 1 ms^{-1}, and the peak currents $\kappa(\hat{t}_i)$ are assumed equal to 19.5 pA. Let us consider a network of $N = 1000$ neurons, each one having excitatory connections to 10 randomly chosen neurons different from itself. The synaptic strengths are then taken to be equal to

$$J_{ij} = \Sigma w_{ij} - \Delta, \tag{36}$$

where $w_{ij} = 1$ if there is an excitatory connection from neuron j to neuron i, 0 otherwise. The value of Σ, therefore, represents the strength of the sparse network of excitatory connections, while that of Δ represents the global inhibition between all the neurons in the network. Note that these quantities should not be confused with Σ and Δ defined in the previous subsection on the Wilson–Cowan model.

As for the previous models, the hysteresis loops are shown in Fig. 16a, this time as a function of the strength of the excitatory connections Σ, separately for different level of the global inhibition Δ. The plots start from $\Sigma = 0$ and increase it up to $\Sigma = 180$ pA over 12 s, then decrease it back to zero over the same amount of time. The number of firings is determined over time bins of 24 ms, and groups of 10 time bins are thereafter taken to compute the average firing rate. In Fig. 16b, the region of bistability is shown, according to the points where the rate becomes larger than 25 Hz when increasing Σ (upper curve) and the points where the rate drops below 25 Hz when decreasing Σ (lower curve). Finally, in Fig. 16c the Fano factor of the rate as is plotted as a function of Δ and Σ. In this case, the model is simulated at fixed values of Δ and Σ, the number of spikes in time bins of varying width is calculated, and finally the Fano factor is computed according to Eq. (1). As previously discussed, the width of the time bin needs to be adequately larger than the autocorrelation time of the rate, and was accordingly set to $\delta_{\mathrm{bin}} = 0.2$–$25.6$ s. The effect of rounding from first- to second-order transition is, therefore, also reproduced in this context.

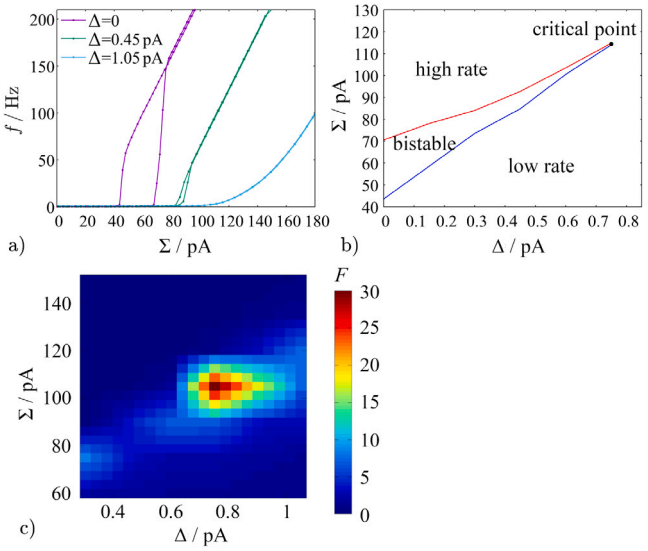

Fig. 16. Simulations of the network of leaky integrate-and-fire neurons. (a) Firing rate during a hysteresis loop of the strength of excitatory connections, for different intensities of global inhibition. (b) Region of bistability in the plane of Δ and Σ. The upper curve denotes where the rate becomes larger than 25 Hz when increasing Σ in the hysteresis loop, whereas the lower curve denotes where the rate drops below 25 Hz when decreasing Σ. (c) Fano factor computed under static conditions.

5.3. Commentary

Albeit briefly, these final simulations underline two important aspects. First, the results obtained from the neon glow lamp system indeed appear to be generalizable to other neural models, reaffirming their relevance to neurophysiology and computational neuroscience. Across all these systems, a critical point is always found as a function of a pair of parameters controlling local excitability and global inhibition strength. In other words, the gradual rounding from a first- to a second-order transition does not stem from a system-specific feature, as was already implied by the results obtained in the mean-field model. Second, the results hold across different scales of neural modeling. Given the sheer size and complexity of biological neural systems, the conjoint consideration of multiple levels of description -both structurally and dynamically- is a cornerstone of modern neuroscience [58–60]. Investigations concerned with the behavior of individual neurons hinge around physiologically-realistic models which, albeit to varying degrees of detail, represent the fundamental aspect of the temporal evolution of spike generation; the leaky integrate-and-fire model is one of the most commonly used abstractions in this area, as it lends itself well to the simulation and training of microscale networks that typically include hundreds to thousands of neurons corresponding, for example, to a cortical microcircuit [56,57]. On the other hand, studies addressing large-scale dynamics, such as those unfolding over extended cortical circuits, necessarily trade physiological detail for computational tractability, and represent entire populations of neurons in an aggregate form through a small number of state variables corresponding, for instance, to the level of activity in excitatory and inhibitory subpopulations. Arguably the most influential model of this class is the Wilson–Cowan model [49,50]. There are countless variations of models of individual neurons and neural masses, encompassing the

non-trivial effects of important factors such as stochastic dynamics [52,53], and greater physiological detail such as the FitzHugh–Nagumo and Hindmarsh–Rose systems [58–60]. The present results only represent an initial confirmation of generality, and a comprehensive assessment of the impact of global inhibitory feedback on neural dynamics using these models is well-motivated but left for others to pursue.

6. Discussion

6.1. Bistability and hysteresis in the present array circuit and other engineered systems

This work was predicated upon the idea of modifying an electronic model of neural dynamics by adding global inhibitory feedback, implemented via an additional resistor. This resistor instantaneously translates an increase of the absorbed current into a decrease of the globally-applied control voltage, which determines how closely each node dwells close to its excitation potential. The principal finding is that this type of feedback, through attenuating the spatiotemporal variance and correlations, has a pronounced effect on the transition between two phases of the collective dynamics, one featuring low rate and low spatiotemporal order, the other characterized by considerably more intense and more regular activity. In line with previous observations, when the additional resistor has zero value, the switchover between the two phases as a function of the control voltage is discontinuous and associated with a relatively large hysteresis effect. There is, in other words, a first-order transition between two well-separated bistable states [39]. As the resistor value is increased, the two states are drawn closer, the bistability shrinks, and the discontinuity becomes rounded, eventually turning into a continuous, second-order transition. Implementing a similar global inhibitory feedback produced analogous effects in two different neural models, pointing to a plausible generality of the observed association, including in biological systems.

At this point, it is worthwhile reminding oneself about the relationship between bistability and hysteresis. Bistability is the presence of two (or more, in the case of multistability) stable states, corresponding to the local minima of a potential function. In the absence of noise, the states have an infinite lifetime, however, in the presence of noise, the lifetimes depend on the depths of corresponding potential wells. Bistability is a necessary condition for hysteresis, and the separation between the two states determines the width of the hysteresis effect [61]. On the other hand, though bistability and hysteresis are often observed together, bistability is not a sufficient condition for hysteresis because, for example, one of the states could be inaccessible under given conditions [62].

Both bistability and hysteresis are common observations in engineered systems, either by design or as a consequence of physical properties, with well-studied examples found in electronics, mechanics and optics. The modeling and control of hysteretic systems is a prominent topic in systems theory, and general operator- and differential-based mathematical models are available [63]. An archetypal example is the Schmitt trigger, which is a buffer designed to exhibit a prescribed hysteresis level acting as a filter and reducing the bouncing of digital signals near the logical threshold [64]. In the case of this circuit, the width of the hysteresis effect is directly determined by a positive feedback gain combined with a saturation function, and, accordingly, several circuits allowing one to change it dynamically have been described [65]. On the other hand, dynamical systems endowed with a double-well potential, as described by the Duffing equation, can also display hysteresis, the width of which is controlled by the potential landscape. For example, in driven mechanical resonators, the bistability region shrinks with increasing dissipation and decreasing driving force [66].

In this paper, a different and novel mechanism leading to a bistable and hysteretic behavior has been considered. As compared with the previous examples, the new mechanism is different because such properties do not stem directly from a design feature: positive feedback in the former case, and potential landscape in the latter. Rather, they emerge from the presence of two phases in a system composed of many interacting constituents and therefore amenable to be studied with the tools of statistical mechanics. In fact, the hysteresis of each individual lamp, which is determined by the difference between the breakdown and extinction voltage and determines the periodic flashing in the Pearson–Anson relaxation oscillator, is fixed by physical construction (e.g., gas mixture composition and pressure, electrode composition and distance) [43]. In the absence of an ensemble of units, an isolated lamp does not show distinct high and low rate phases, therefore, there is no hysteresis or bistability in the event rate, and fluctuations are Poissonian. It is only the interactions between many lamps that lead to collective states characterized by different event rates, and eventually to the large fluctuations and non-Poissonian behavior when approaching the critical point. In the settings considered here, the behavior of the system could be well described by a simple approximation where the interaction between the lamps is a long-range one and mediated by a "mean field", represented by the variance of the local potentials of the lamps [39]. It has to be stressed that the phase transition observed is different from a thermodynamical phase transition, in the sense that the system considered cannot be straightforwardly described by an energy function, and its phases by the minima of the free energy. Rather, it is a non-equilibrium phase transition between different states of the system, characterized by non-zero currents and dissipation. However, an analogy with thermodynamic phase transitions is possible in the limit of a large number of constituents and slow (quasi-static) variation of the external parameters [47,67,68].

6.2. Comparison with other physical scenarios

Physical systems abound in situations where first- and second-order phase transitions appear in different regions of the parameter space. Such transitions could be juxtaposed to the observations in dynamical systems such as the present circuit under two assumptions, namely, that the system behaves sufficiently close to the infinite-dimensional case and that the process is quasi-static [47]. Because dynamical systems, by contrast, inherently operate far from equilibrium, the juxtaposition can be proposed purely at a phenomenological level [67,68]. In classical thermodynamics, the transitions between the macroscopic phases of matter away from the critical point are first-order, eventually turning into second-order as the critical point is reached. Increasing temperature, therefore, can lead to a shrinkage of the hysteresis effect akin to increasing resistance in the present system [69]. In ferromagnetic materials, the bulk magnetization vs. the magnetizing field shows a well-known hysteresis effect, the width of which depends foremost on the type of material. For increasing temperature, the disorder induced by thermal activation causes a shrinkage of the loop, until, at the critical temperature, the transition becomes second-order [70]. The dependence of coercivity on temperature is explicitly described by Kneller's law [71].

Besides, the notion that a first-order transition may turn into a second-order one through gradual rounding of the discontinuity has been repeatedly put forward across diverse situations; for instance, random fluctuations in the structural parameters suppress first-order transitions in ferromagnetic random-field Ising spin models [72] and in magnetoresistive manganites [73]. Changeover between first- and second-order transitions has also been described as a function of the number of states in generalizations of the Ising model [74], and as a function of an electromagnetic field applied to a population of two-level atoms [75]. Under suitable conditions, in liquid crystals, increasing temperature, due to its effects on domain size, leads to a first-order phase transition eventually being replaced by a second-order one [76]. An effect of the interaction range on the transition order is also observed in spatial interdependent networks, wherein couplings beyond

a minimal range are required for first-order transitions to appear [77], and in models of synchronization and swarming behaviors [78]. There is, therefore, a multitude of known physical scenarios within which a secondary control parameter modulates, in a reversible way, the separation between bistable states and eventually the transition order observed as a function of a primary control parameter.

6.3. Possible biological mechanisms of global inhibition

Two aspects remain to be discussed: the mechanisms through which global inhibitory feedback could be implemented in biological neural systems, and the computational role that it could serve in that context.

The existence of synaptic architectures that implement global inhibition has been postulated for a range of neural functions, and explicitly demonstrated in specific cases, most notably the head-direction cell circuit [13]. While the actual biological realization is likely to be more complex and detailed accounts of interneuron diversity and connectivity are found elsewhere [4,5], three stylized motifs implementing global inhibition can be envisaged. The first revolves around a single large interneuron enjoying both high indegree and outdegree, and forming synapses directly with many excitatory cells to integrate spatiotemporally their activity and feed back a diffuse inhibition signal. The presence of this motif has been directly demonstrated in the mouse visual thalamus using high-resolution reconstruction of neural morphology [11]. The second involves the distributed action of a large number of interneurons that, while individually having fewer processes, collectively parcel out an extended region, potentially forming intertwined, interacting, or even competing connections. In a broad sense, this is the arrangement realized by the ring and δ neurons in head-direction circuits [13–15]. The third is based on local interneurons endowed with high in-degree, attained either through direct connections or mediated by other neurons, that gather excitatory activity in a diffuse and unspecific form, then apply an excitatory signal on specific targets, thus having a relatively low outdegree. This architecture is the one that is deemed fundamental towards realizing sparse responses encoding odors across glomeruli in insects, as visualized by both calcium imaging and electrical recordings [16,17].

It needs to be considered that synaptic architectures are not the only mechanism by which global inhibition could be implemented in biological neural systems, since numerous other feedback mechanisms are present. An important aspect to consider is the interaction between neurons and glial cells, particularly astrocytes, that have long been known to exert a regulatory action via inhibition [79]. In particular, astrocytic processes envelope synapses, leading to the notion of "tripartite" synapses, and this is drawing considerable attention because it appears to subserve not only a homeostatic but also potentially a computational function [80,81]. A multitude of biochemical pathways have been described, providing the ability for astrocytes to both sense the concentration of and release the primary inhibitory neurotransmitter released by interneurons, gamma-aminobutyric acid, thus effectively mimicking their action [82,83]. Remarkably, depending on the species, a single astrocyte can directly contact thousands or millions of synapses, forming anatomical domains that parcel the cortex in an organized manner, implying a certain level of functional specificity [84,85]. Furthermore, it was demonstrated that astrocytes control the dynamic range of neural activity, continuously adjusting the circuit gain and spike timing to optimize the responsiveness to sensory stimuli of different intensities, and influencing the behaviors that these produce. Their action, therefore, appears to have substantial elements of similarity with that of interneurons [86,87].

Another key pathway for global inhibition is the regulation of the extracellular ionic concentrations, which track the spatiotemporal summation of neural activity, and, in turn, exert a diffuse influence on the level of excitability. All types of glia appear to be potentially implicated in the dynamic regulation of potassium levels, with some diversity depending on the brain region [88]. Astrocytes, in particular, have a central role in this mechanism, providing a signaling medium suitable for information distribution [89,90]. In turn, they form extended networks between themselves via gap junctions, providing a further means of interaction [91]. Specialized types of glia in the cerebellum even show dynamic uptake of potassium under the control of calcium transients, closely resembling proper synaptic functions. There are, therefore, a multitude of mechanisms through which glia could implement global inhibition [92].

6.4. Significance and future work

As said, the joint action of local excitation and global inhibition has been posited to be a fundamental substrate for a multitude of neural functions, including implementing ring attractor dynamics in head direction circuits [13–15], enabling a sparsely coded representation of odors across glomeruli [16,17], modulating the range of memory retrieval [19], and controlling the network-level signal amplification and switchover between dynamical regimes [20]. A particularly compelling computational model based on global inhibition and local excitation is known as the "Locally Excitatory Globally Inhibitory Oscillator Networks (LEGION)", and was found to have excellent performance in solving specific signal processing problems, such as image segmentation [93]. The point of the present work, however, is different and revolves more specifically around the notion that global inhibitory feedback gradually rounds a discontinuous transition, shrinking the region of bistability and hysteresis and turning the transition into a continuous one. In particular, there appears to be a combination of local excitability and global inhibition strength that corresponds to a critical point. Why would such a mechanism be relevant to the brain? We posit that an ability to dynamically switch between dynamics characterized by first- and second-order transitions is essential, because hysteresis is necessary, for example, for sensory and memory persistence [22–24], while operation close to criticality advantageously optimizes dynamical range, information capacity, and flexibility [28,32–36].

Future work should investigate in biological scenarios the postulated relevance of global inhibition in controlling the transition order. In this regard, a very recent study based on stereo-electroencephalography in epilepsy patients and computational modeling concluded that in the brain critical-like dynamics emerge over a continuum between first- and second-order phase transitions. A fact of particular interest is that positive feedback promoted the bistable dynamics, which rhymes with the present observation that negative feedback, by contrast, attenuates discontinuity [25]. In-vitro recordings of cultured neurons and brain slices using multi-electrode arrays provide access to a rich repertoire of spontaneous behaviors [29,94], and optogenetics provides a versatile tool to implement global inhibition [95]. Combining the two techniques in a closed-loop configuration, therefore, appears motivated to replicate the present work in a biological setting. A suggested setup for a future experiment is shown in Fig. 17, and involves interfacing a neural culture on a multi-electrode array to a real-time digital signal processor, that would perform spike detection and spatiotemporal activity summation. The activity level thus determined would be multiplied by a gain controlling the intensity of global inhibition, which would be delivered nearly instantaneously via an optical signal through a light-emitting diode, thus realizing a closed-loop control referred to as Path #1. The possibility of processing neural signals of this kind with sub-millisecond latencies using programmable logic has been shown before [96], and the inhibition could be delivered biologically either through interneuron activation, or through the hyperpolarization of excitatory neurons using an opsin such as halorhodopsin (a chloride pump activated by yellow light). The sweep in the baseline excitability level could be realized via another open-loop path, referred to as Path #2. One possibility would be to implement dual optogenetic control, for example via inducing depolarization through the activation of channelrhodopsin (a nonspecific cation channel activated by blue light) [97]. It is important to underline that, while Path #1 would

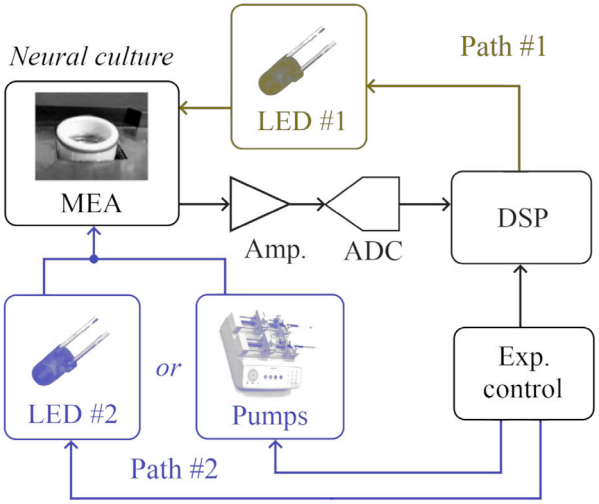

Fig. 17. Hypothetical setup for an experimental investigation in cultured neurons. Path #1 delivers the real-time global inhibitory feedback, while Path #2 provides the parametric sweep to investigate hysteresis. ADC: Analog-to-digital converter, DSP: Digital signal processor, MEA: Multi-electrode array. See text for description.

provide a high-speed pulsed feedback signal, Path #2 would provide a continuous, quasi-static illumination to slowly perform a parametric sweep, as done for the supply voltage in the neon lamp array in this paper. Given the need for only slow changes, replacing the culture medium continuously using a flow chamber-like approach would be another possibility. In such a case, one could start with a Ca^{2+}-free medium, gradually increase its concentration, and then flush it away, or similarly work on the concentrations of Na^{+} and K^{+}.

CRediT authorship contribution statement

Ludovico Minati: Conceptualization, Investigation, Methodology, Software, Writing – original draft. **Silvia Scarpetta:** Conceptualization, Investigation, Methodology, Software, Writing – original draft. **Mirna Andelic:** Writing – original draft. **Pedro A. Valdes-Sosa:** Writing – review & editing. **Leonardo Ricci:** Writing – review & editing. **Antonio de Candia:** Conceptualization, Formal analysis, Investigation, Methodology, Software, Writing – original draft.

Declaration of competing interest

The authors declare that they have no known competing financial interests or personal relationships that could have appeared to influence the work reported in this paper.

Data availability

The time series recorded from the analog circuits are downloadable from http://dx.doi.org/10.5281/zenodo.10585140.

Acknowledgments

L.M. gratefully acknowledges the support of the “Hundred Talents” program of the University of Electronic Science and Technology of China, and the support of the “Excellent Young Scientists Fund Program (Overseas)” program of the National Natural Science Foundation of China. All experimental activities were self-funded and conducted by L.M. during the period 2020–2021 using own independent assets located in Grigno TN, Italy; the manuscript was later finalized after joining the University of Electronic Science and Technology of China, to which no equipment was transferred. This work has been supported by the Chengdu Science and Technology Bureau Program, China under Grant 2022GH02-00042-HZ and the CNS program of UESTC, China No. Y0301902610100201. The authors are grateful to Gabriele Brugnoni of DVE Progettazione Elettronica (Casciago VA, Italy) for essential workshop and manufacturing support.

References

[1] Kandel E, Koester JD, Mack SH. Principles of neural science. Columbus OH, USA: McGraw-Hill Education; 2021.
[2] Wingert JC, Sorg BA. Impact of perineuronal nets on electrophysiology of parvalbumin interneurons, principal neurons, and brain oscillations: A review. Front Synaptic Neurosci 2021;13:673210.
[3] McBain CJ, Fisahn A. Interneurons unbound. Nat Rev Neurosci 2001;2:11–23.
[4] Fishell G, Kepecs A. Interneuron types as attractors and controllers. Annu Rev Neurosci 2020;43:1–30.
[5] Kepecs A, Fishell G. Interneuron cell types: Fit to form and formed to fit. Nature 2014;505(7483):318–26.
[6] Luhmann HJ. Dynamics of neocortical networks: connectivity beyond the canonical microcircuit. Pflugers Arch 2023;475:1027–33.
[7] van Vreeswijk C, Sompolinsky H. Chaos in neuronal networks with balanced excitatory and inhibitory activity. Science 1996;274(5293):1724–6.
[8] Sohal VS, Rubenstein JLR. Excitation-inhibition balance as a framework for investigating mechanisms in neuropsychiatric disorders. Mol Psychiatry 2019;24:1248–57.
[9] Trinchero MF, Giacomini D, Schinder AF. Dynamic interplay between Gabaergic networks and developing neurons in the adult hippocampus. Curr Opin Neurobiol 2021;69:124–30.
[10] Nashef A, Cohen O, Perlmutter SI, Prut Y. A cerebellar origin of feed-forward inhibition to the motor cortex in non-human primates. Cell Rep 2022;39(6):110803.
[11] Morgan JL, Lichtman JW. An individual interneuron participates in many kinds of inhibition and innervates much of the mouse visual thalamus. Neuron 2020;106(3):468–81.
[12] Mysore SP, Asadollahi A, Knudsen EI. Global inhibition and stimulus competition in the owl optic tectum. J Neurosci 2010;30:1727–38.
[13] Kim SS, Rouault H, Druckmann S, Jayaraman V. Ring attractor dynamics in the drosophila central brain. Science 2017;356(6340):849–53.
[14] Tanaka H, Nelson DR. Non-Hermitian quasilocalization and ring attractor neural networks. Phys Rev E 2019;99:062406.
[15] Chang N, Huang H-P, Lo C-C. Global inhibition in head-direction neural circuits: a systematic comparison between connectome-based spiking neural circuit models. J Comp Physiol A 2023;209:721–35.
[16] Poo C, Isaacson JS. Odor representations in olfactory cortex: Sparse coding, global inhibition, and oscillations author links open overlay panel. Neuron 2009;62(6):850–61.
[17] Silbering AF, Galizia CG. Processing of odor mixtures in the Drosophila antennal lobe reveals both global inhibition and glomerulus-specific interactions. J Neurosci 2007;27(44):11966–77.
[18] Scarpetta S, De Candia A. Information capacity of a network of spiking neurons. Physica A 2019;545:123681.
[19] Burns TF, Haga T, Fukai T. Multiscale and extended retrieval of associative memory structures in a cortical model of local-global inhibition balance. eNeuro 2022;9(3):23.
[20] Christodoulou G, Vogels TP, Agnes EJ. Regimes and mechanisms of transient amplification in abstract and biological neural networks. PLoS Comput Biol 2022;18(8):e1010365.
[21] Buice MA, Cowan JD. Statistical mechanics of the neocortex. Prog Biophys Mol Biol 2009;99(2–3):53–86.
[22] Durstewitz D, Seamans JK, Sejnowski TJ. Neurocomputational models of working memory. Nat Neurosci 2000;3:1184–91.
[23] Brody CD, Romo R, Kepecs A. Basic mechanisms for graded persistent activity: discrete attractors, continuous attractors, and dynamic representations. Curr Opin Neurobiol 2003;13(2):204–11.
[24] Schwiedrzik CM, Ruff CC, Lazar A, Leitner FC, Singer W, Melloni L. Untangling perceptual memory: hysteresis and adaptation map into separate cortical networks. Cereb Cortex 2014;24(5):1152–64.
[25] Wang SH, Siebenhühner, Arnulfo G, Myrov V, Nobili L, Breakspear M, Palva S, Palva JM. Critical-like brain dynamics in a continuum from second to first-order phase transition. J Neurosci 2023;43(45):7642–56.
[26] Leow MK-S. A review of the phenomenon of hysteresis in the hypothalamus–pituitary–thyroid axis. Front Endocrinol 2016;7:64.
[27] Kim H, Moon J-Y, Mashour GA, Lee U. Mechanisms of hysteresis in human brain networks during transitions of consciousness and unconsciousness: Theoretical principles and empirical evidence. PLoS Comput Biol 2018;14(8):e1006424.

[28] Beggs JM, Plenz D. Neuronal avalanches in neocortical circuits. J Neurosci 2003;23(35):11167–77.
[29] Tetzlaff C, Okujeni S, Egert U, Wörgötter F, Butz M. Self-organized criticality in developing neuronal networks. PLoS Comp Biol 2010;6(12):e1001013.
[30] Friedman N, Ito S, Brinkman BAW, Shimono M, Lee DeVille RE, Dahmen KA, Beggs JM, Butler TC. Universal critical dynamics in high resolution neuronal avalanche data. Phys Rev Lett 2012;108:208102.
[31] Tagliazucchi E, Balenzuela P, Fraiman D, Chialvo DR. Criticality in large-scale brain fMRI dynamics unveiled by a novel point process analysis. Front Physiol 2012;3:15.
[32] Kinouchi O, Copelli M. Optimal dynamical range of excitable networks at criticality. Nat Phys 2006;2:348–51.
[33] Levina A, Herrmann JM, Geisel T. Phase transitions towards criticality in a neural system with adaptive interactions. Phys Rev Lett 2009;102:118110.
[34] Chialvo DR. Emergent complex neural dynamics. Nat Phys 2010;6:744–50.
[35] Shew WL, Yang H, Yu S, Roy R, Plenz D. Information capacity and transmission are maximized in balanced cortical networks with neuronal avalanches. J Neurosci 2011;31(1):55–63.
[36] Scarpetta S, de Candia A. Neural avalanches at the critical point between replay and non-replay of spatiotemporal patterns. PLoS ONE 2013;8(6):e64162.
[37] Haldeman C, Beggs JM. Critical branching captures activity in living neural networks and maximizes the number of metastable states. Phys Rev Lett 2005;94:058101.
[38] Tognoli E, Kelso JAS. The metastable brain. Neuron 2014;81(1):35–48.
[39] Minati L, de Candia A, Scarpetta S. Critical phenomena at a first-order phase transition in a lattice of glow lamps: Experimental findings and analogy to neural activity. Chaos 2016;26:073103.
[40] Scarpetta S, Apicella I, Minati L, De Candia A. Hysteresis, neural avalanches, and critical behavior near a first-order transition of a spiking neural network. Phys Rev E 2018;97:062305.
[41] Dougherty CR, Foulke TD, Harden JD, Hewitt T, Peters FN, Smith RD, Tuttle JW. Glow lamp manual. Cleveland, OH, USA: General Electric Company; 1966.
[42] van der Pol B, van der Mark J. Frequency demultiplication. Nature 1927;120(3019):363–4.
[43] Pearson SO, Anson HSG. The neon tube as a means of producing intermittent currents. Proc R Soc Lond Ser A Math Phys Eng Sci 1921;34:204.
[44] Time series recorded from the experimental apparatus downloadable from [link to be inserted].
[45] Fano U. Ionization yield of radiations. II. The fluctuations of the number of ions. Phys Rev 1947;72:26–9.
[46] Rajdl K, Lansky P, Kostal L. Fano factor: A potentially useful information. Front Comput Neurosci 2020;14:569049.
[47] Huang K. Introduction to statistical physics. Boca Raton FL, USA: CRC Press; 2009.
[48] Kolmogorov AN. Statistical theory of nucleation processes. Bull Acad Sci USSR Math Ser 1937;3:355.
[49] Wilson HR, Cowan JD. Excitatory and inhibitory interactions in localized populations of model neurons. Biophys J 1972;12:1.
[50] Destexhe A, Sejnowski TJ. The Wilson–Cowan model, 36 years later. Biol Cybern 2009;101(1):1–2.
[51] van Kampen NG. Stochastic processes in physics and chemistry. Amsterdam, The Netherlands: North Holland; 2007.
[52] Benayoun M, Cowan JD, van Drongelen W, Wallace E. Avalanches in a stochastic model of spiking neurons. PLoS Comput Biol 2010;6:e1000846.
[53] De Candia A, Sarracino A, Apicella I, de Arcangelis L. Critical behaviour of the stochastic Wilson–Cowan model. PLoS Comput Biol 2021;17(8):e1008884.
[54] Sarracino A, Arviv O, Shriki O, de Arcangelis L. Predicting brain evoked response to external stimuli from temporal correlations of spontaneous activity. Phys Rev Res 2020;2:033355.
[55] Risken H. The Fokker–Planck equation. Berlin, Germany: Springer; 1996.
[56] Lansky P, Sanda P, He J. The parameters of the stochastic leaky integrate-and-fire neuronal model. J Comput Neurosci 2006;21(2):211–23.
[57] Burkitt AN. A review of the integrate-and-fire neuron model: I. Homogeneous synaptic input. Biol Cybern 2006;95(1):1–19.
[58] Buzsáki G, Christen Y, editors. Micro-, meso- and macro-dynamics of the brain. Cham, Switzerland: Springer; 2016.
[59] Ramezanian-Panahi M, Abrevaya G, Gagnon-Audet J-C, Voleti C, Rish I, Dumas G. Generative models of brain dynamics. Front Artif Intell 2022;5:807406.
[60] D'Angelo E, Jirsa V. The quest for multiscale brain modeling. Trends Neurosci 2022;45(10):777–90.
[61] Bonifacio R, Lugiato LA. Optical bistability and cooperative effects in resonance fluorescence. Phys Rev A 1978;18:1129.
[62] Guidi GM, Goldbeter A. Bistability without hysteresis in chemical reaction systems: A theoretical analysis of irreversible transitions between multiple steady states. J Phys Chem A 1997;101(49):9367–76.
[63] Hassani V, Tjahjowidodo T, Nho Do T. A survey on hysteresis modeling, identification and control. Mech Syst Signal Process 2014;49(1–2):209–33.
[64] Horowitz P, Hill W. The art of electronics. Cambridge, UK: Cambridge University Press; 2015.
[65] Sukhwani M, Chandratre VB, Thomas M, Prasad HK, Kesarkar T. A high speed BiCMOS comparator ASIC with voltage adjustable hysteresis. Nucl Instrum Methods Phys Res A 2020;980:164503.
[66] Schmid S, Villanueva LG, Roukes ML. Fundamentals of nanomechanical resonators. Cham, Switzerland: Springer; 2016.
[67] Haken H. Cooperative phenomena in systems far from thermal equilibrium and in nonphysical systems. Rev Modern Phys 1975;47:67.
[68] Synergetics Haken H. An introduction: non-equilibrium phase transitions and self-organization in physics, chemistry and biology. Berlin, Germany: Springer; 1977.
[69] Klein S, Nellis G. Thermodynamics. Cambridge, UK: Cambridge University Press; 2011.
[70] Bozorth RM. Ferromagnetism. Piscataway NJ, USA: Wiley-IEEE Press; 1993.
[71] Kneller EF, Luborsky FE. Particle size dependence of coercivity and remanence of single-domain particles. J Appl Phys 1963;34:656–8.
[72] Aizenman M, Wehr J. Rounding of first-order phase transitions in systems with quenched disorder. Phys Rev Lett 1989;62:2503.
[73] Rößler S, Rößler UK, Nenkov K, Eckert D, Yusuf SM, Dörr K, Müller K-H. Rounding of a first-order magnetic phase transition in Ga-doped La0.67Ca0.33MnO3. Phys Rev B 2004;70:104417.
[74] Yagiz Devre H, Nihat Berker A. First-order to second-order phase transition changeover and latent heats of q-state potts models in d=2, 3 from a simple Migdal–Kadanoff adaptation. Phys Rev E 2022;105:054124.
[75] Bowden CM, Sung CC. First- and second-order phase transitions in the Dicke model: Relation to optical bistability. Phys Rev A 1979;19:2392.
[76] Emelyanenko AV, Rudyak VY, Shvetsov SA, Araoka F, Nishikawa H, Ishikawa K. Emergence of paraelectric, improper antiferroelectric, and proper ferroelectric nematic phases in a liquid crystal composed of polar molecules. Phys Rev E 2022;105:064701.
[77] Gross B, Bonamassa I, Havlin S. Dynamics of cascades in spatial interdependent networks. Chaos 2023;33(10):103116.
[78] Kongni SJ, Nguefoue V, Njougouo T, Louodop P, Fagundes Ferreira F, Tchitnga R, Cerdeira HA. Phase transitions on a multiplex of swarmalators. Phys Rev E 2023;108:034303.
[79] Héja L, Nyitrai G, Kékesi O, Dobolyi A, Szabó P, Fiáth R, Ulbert I, Pál-Szenthe B, Palkovits M, Kardos J. Astrocytes convert network excitation to tonic inhibition of neurons. BMC Biol 2012;10:26.
[80] Allen NJ, Eroglu C. Cell biology of astrocyte-synapse interactions. Neuron 2017;96(3):697–708.
[81] Liu Y, Shen X, Zhang Y, Zheng X, Cepeda C, Wang Y, Duan S, Tong X. Interactions of glial cells with neuronal synapses, from astrocytes to microglia and oligodendrocyte lineage cells. Glia 2023;71(6):1383–401.
[82] Yoon BE, Woo J, Justin Lee C. Astrocytes as GABA-ergic and GABA-ceptive cells. Neurochem Res 2012;37:2474–9.
[83] Liu J, Feng X, Wang Y, Xia X, Zheng JC. Astrocytes: Gabaceptive and Gabaergic cells in the brain. Front Cell Neurosci 2022;6:892497.
[84] Bushong EA, Martone ME, Jones YZ, Ellisman MH. Protoplasmic astrocytes in CA1 stratum radiatum occupy separate anatomical domains. J Neurosci 2002;22(1):183–92.
[85] Oberheim NA, Takano T, Han X, He W, Lin JHC, Wang F, Xu Q, Wyatt JD, Pilcher W, Ojemann JG, Ransom BR, Goldman SA, Nedergaard M. Uniquely hominid features of adult human astrocytes. J Neurosci 2009;29(10):3276–87.
[86] Kwak H, Koh W, Kim S, Song K, Shin J-I, Lee JM, Lee EH, Bae JY, Ha GE, Oh J-E, Park YMason, Kim S, Feng J, Lee SE, Choi JW, Kim KE, Kim YS, Woo J, Lee D, Son T, Kwon SW, Park KD, Yoon B-E, Lee J, Li Y, Lee H, Bae YC, Lee CJ, Cheong E. Astrocytes control sensory acuity via tonic inhibition in the thalamus. Neuron 2020;108(4):691–706.
[87] Miguel-Quesada C, Zaforas M, Herrera-Pérez S, Lines J, Fernández-López E, Alonso-Calviño E, Ardaya M, Soria FN, Araque A, Aguilar J, Rosa JM. Astrocytes adjust the dynamic range of cortical network activity to control modality-specific sensory information processing. Cell Rep 2023;42(8):112950.
[88] Larsen BR, Assentoft M, Cotrina ML, Hua SZ, Nedergaard M, Kaila K, Voipio J, N. MacAulay. Contributions of the Na+/K+-ATPase, NKCC1, and Kir4.1 to hippocampal K+ clearance and volume responses. Glia 2014;62(4):608–22.
[89] Laming PR. Potassium signalling in the brain: its role in behaviour. Neurochem Int 2000;36(4–5):271–90.
[90] Hertz L, Chen Y. Importance of astrocytes for potassium ion (K+) homeostasis in brain and glial effects of K+ and its transporters on learning. Neurosci Biobehav Rev 2016;71:484–505.
[91] Houades V, Koulakoff A, Ezan P, Seif I, Giaume C. Gap junction-mediated astrocytic networks in the mouse barrel cortex. J Neurosci 2008;28(20):5207–17.

[92] Wang F, Xu Q, Wang W, Nedergaard M. Bergmann glia modulate cerebellar purkinje cell bistability via Ca2+-dependent K+ uptake. Proc Natl Acad Sci USA 2012;109(20):7911–6.

[93] Terman D, Wang DL. Global competition and local cooperation in a network of neural oscillators. Physica D 1995;81:148–76.

[94] Wagenaar DA, Pine J, Potter SM. An extremely rich repertoire of bursting patterns during the development of cortical cultures. BMC Neurosci 2006;7:11.

[95] Ledri M, Gronning Madsen M, Nikitidou L, Kirik D, Kokaia M. Global optogenetic activation of inhibitory interneurons during epileptiform activity. J Neurosci 2014;34(9):3364–77.

[96] Seu GP, Angotzi GN, Boi F, Raffo L, Berdondini L, Meloni P. Exploiting all programmable SoCs in neural signal analysis: A closed-loop control for large-scale CMOS multielectrode arrays. IEEE Trans Biomed Circuits Syst 2018;12:839–50.

[97] Warden MR, Cardin JA, Deisseroth K. Optical neural interfaces. Annu Rev Biomed Eng 2014;16:103–29.